ARTICLE

ESCRT-III–mediated membrane fusion drives chromosome fragments through nuclear envelope channels

Brandt Warecki⬤, Xi Ling⬤, Ian Bast⬤, and William Sullivan⬤

Mitotic cells must form a single nucleus during telophase or exclude part of their genome as damage-prone micronuclei. While research has detailed how micronuclei arise from cells entering anaphase with lagging chromosomes, cellular mechanisms allowing late-segregating chromosomes to rejoin daughter nuclei remain underexplored. Here, we find that late-segregating acentric chromosome fragments that rejoin daughter nuclei are associated with nuclear membrane but devoid of lamin and nuclear pore complexes in *Drosophila melanogaster*. We show that acentrics pass through membrane-, lamin-, and nuclear pore–based channels in the nuclear envelope that extend and retract as acentrics enter nuclei. Membrane encompassing the acentrics fuses with the nuclear membrane, facilitating integration of the acentrics into newly formed nuclei. Fusion, mediated by the membrane fusion protein Comt/NSF and ESCRT-III components Shrub/CHMP4B and CHMP2B, facilitates reintegration of acentrics into nuclei. These results suggest a previously unsuspected role for membrane fusion, similar to nuclear repair, in the formation of a single nucleus during mitotic exit and the maintenance of genomic integrity.

Introduction

The goal of mitosis is to produce two genetically identical daughter cells. Failure to undergo accurate mitosis results in aneuploidy and the loss of key genetic information. To guarantee accurate production of daughters, cells have evolved mechanisms ensuring proper genome replication and segregation. However, simply segregating sister chromatids equally to each daughter cell is insufficient to maintain euploidy. Instead, the entire segregating chromosome complement must also be gathered into a single daughter nucleus (Zhang et al., 2015; Ly et al., 2017; Samwer et al., 2017). Failure to form a single nucleus results in the formation of one or more micronuclei, unstable structures that can undergo chromothripsis, a type of catastrophic DNA damage in which the micronuclear DNA is shattered, rearranged, and then reincorporated into the genome (Stephens et al., 2011; Crasta et al., 2012; Zhang et al., 2015; Ly et al., 2017). Chromothripsis results in aneuploidy (Zhang et al., 2015). Multiple studies link chromothripsis to the development and progression of cancer, and the presence of micronuclei has long been considered a hallmark of cancer cells (Stephens et al., 2011; Santos et al., 2010; Bonassi et al., 2011).

Lagging of whole or fragmented chromosomes during anaphase is perhaps the most common origin of micronuclei (Fenech et al., 2011). Lagging chromosomes can be "locked out" of daughter nuclei if they remain distinct from the main nuclei at the time when the nuclear envelope reassembles around the main chromosome complement. During nuclear envelope reassembly, nuclear membrane is recruited to chromatin, the nuclear lamina is reestablished, and nuclear pore complexes reform. Different domains of nuclear membrane are then sealed together via the action of conserved membrane fusion proteins such as NSF and the ESCRT (endosomal sorting complexes required for transport)-III complex (Baur et al., 2007; Vietri et al., 2015; Olmos et al., 2015). The reassembled nuclear envelope would be expected to act as a physical barrier that prevents lagging chromosome entry into the daughter nucleus and therefore contributes to the formation of a micronucleus.

While lagging chromosomes certainly pose a significant risk to the genetic integrity of a dividing cell, in actuality, not every lagging chromosome is destined to form a micronucleus. In some instances, lagging chromosomes enter telophase daughter nuclei, preserving euploidy. For example, lagging whole chromosomes can rejoin daughter nuclei in human colorectal cancer cells (Huang et al., 2012) and fission yeast (Pidoux et al., 2000; Sabatinos et al., 2015). In addition, late-segregating acentric

Department of Molecular, Cell, and Developmental Biology, University of California, Santa Cruz, Santa Cruz, CA.

Correspondence to William Sullivan: sullivan@biology.ucsc.edu.

fragments sometimes rejoin daughter nuclei in cultured mammalian cells (Liang et al., 1993) and several insect species, including *Chortophaga viridifasciata* (Carlson, 1938) and *Drosophila melanogaster* (Royou et al., 2010; Bretscher and Fox, 2016).

These examples suggest the presence of mechanisms that alter normal mitotic events to allow the inclusion of late-segregating chromatids into daughter nuclei, maintaining genome integrity. While many studies have documented how a micronucleus could contribute to genomic instability (Terradas et al., 2009, 2012; Crasta et al., 2012; Hatch et al., 2013; Zhang et al., 2015; Ly et al., 2017; de Castro et al., 2017; Maass et al., 2018; Liu et al., 2018), the mechanisms that instead facilitate incorporation of lagging chromosomes into daughter nuclei to maintain euploidy remain underexplored. Here, we address this issue by studying the reintegration of late-segregating acentric chromosome fragments in *Drosophila* neuroblast divisions, which rejoin daughter nuclei with high fidelity (Royou et al., 2010; Kotadia et al., 2012; Karg et al., 2015, 2017; Warecki and Sullivan, 2018).

Acentric behavior in *Drosophila* can be studied with transgenic flies containing a heat shock–inducible I-CreI endonuclease (Rong et al., 2002). I-CreI generates double-stranded DNA breaks in the ribosomal DNA repeats at the base of the X chromosome and results in fragments with persistent γH2Av foci that are incapable of recruiting key kinetochore components and are therefore truly acentric (Royou et al., 2010). Despite lacking a centromere, acentrics undergo a delayed but successful poleward segregation, mediated by a protein-coated DNA tether that connects the acentrics to the main chromosome mass (Royou et al., 2010) and microtubules that enrich in bundles around the segregating acentric (Karg et al., 2017). Because sister separation of the acentrics is significantly delayed, by the time acentrics begin their initial segregation poleward, the nuclear envelope has already begun to reform on daughter nuclei (Karg et al., 2015). This nascent nuclear envelope should act as a barrier to prevent acentric entry into daughter nuclei. Instead, the presence of acentrics and their associated tether triggers the formation of highly localized channels in the nuclear envelope through which the acentrics pass to rejoin daughter nuclei (Karg et al., 2015). Because of the extreme delay in acentric segregation, channels persist for several minutes after they form to allow acentric entry (Karg et al., 2015). During this time the acentric and tether remain free of lamin and nuclear pore complexes (Karg et al., 2015)

Failure to undergo lamin reassembly on late-segregating acentrics could be explained by a spatiotemporal mechanism that blocks nuclear envelope reassembly on chromosomes near the midzone (Afonso et al., 2014; Liu et al., 2018). However, while these spatiotemporal models might justify the lack of lamin assembly on acentrics, which are near the midzone, they cannot account for the formation of nuclear envelope channels on daughter nuclei, which are near the poles. Instead, acentric segregation, channel formation, and incorporation into daughter nuclei rely on the tethers connecting acentrics to their centric partners (Royou et al., 2010). The tether is associated with Polo, BubR1, and the chromosome passenger complex proteins Aurora B and INCENP (Royou et al., 2010). Nuclear envelope channel

formation is dependent on the Aurora B kinase activity associated with the acentric and DNA tether. When Aurora B activity is reduced, channel formation fails even though the tether remains intact (Karg et al., 2015). Consequently, acentrics are unable to enter daughter nuclei and instead form lamin-coated micronuclei. These data demonstrate that channel formation is mediated by localized Aurora B activity on the tether (Warecki and Sullivan, 2018) as opposed to a physical blockage of nuclear envelope assembly by the tether. We note that this model of channel formation on daughter nuclei is not mutually exclusive to the spatiotemporal models that could prevent lamin assembly on the lagging acentric chromatin.

These studies (Afonso et al., 2014; Karg et al., 2015; Warecki and Sullivan, 2018) suggest that nuclear envelope reassembly is inhibitive to acentric entry into daughter nuclei. This view is supported by evidence that inappropriate nuclear envelope reassembly can lead to chromosome segregation defects (Champion et al., 2019) and micronucleus formation (Samwer et al., 2017). While the formation of channels is clearly important to allow acentrics to bypass the physical barrier of the nuclear envelope, the extent to which nuclear envelope reassembly contributes positively to acentric entry is unknown. Here, we show that processes involved in nuclear envelope reassembly promote acentric entry into nuclei. We find that the nuclear envelope channel is highly dynamic, extending outward to reach toward segregating acentrics and retracting back as acentrics enter channels. We find that acentrics reintegrating into daughter nuclei recruit nuclear envelope membrane despite lacking lamin and nuclear pore complexes (Afonso et al., 2014; Karg et al., 2015). In addition, we find that the conserved membrane fusion protein Comt/NSF and the ESCRT-III components Shrub/charged multivesicular body protein 4B (CHMP4B) and CHMP2B are required for efficient entry of acentrics into daughter nuclei. Taken together, these results suggest a novel mechanism for nuclear membrane fusion in maintaining genome integrity, in which fusion between membrane on acentrics and membrane on daughter nuclei guides poleward-segregating acentrics through nuclear envelope channels and into daughter nuclei.

Results

Late-segregating acentrics reach daughter nuclei after nuclear envelope reassembly

Despite lacking kinetochores, I-CreI–induced acentrics ultimately segregate and enter daughter nuclei (Royou et al., 2010). Acentric segregation is so severely delayed that components of the nuclear envelope already begin to localize to the main daughter nuclei while acentrics are still segregating poleward, which should act as a barrier to prevent acentric entry (Karg et al., 2015). We have previously shown that acentrics are able to bypass this barrier by entering through channels in the nascent nuclear envelope surrounding daughter nuclei (Karg et al., 2017).

To more precisely time acentric segregation with respect to nuclear envelope reassembly, we imaged live *Drosophila* neuronal stem cells (neuroblasts) from third-instar larvae expressing

Warecki et al.
ESCRT-III drives chromosome fragments into nuclei

Journal of Cell Biology 2 of 22
https://doi.org/10.1083/jcb.201905091

H2Av-RFP and GFP-NLS, with or without I-CreI expression. The presence of GFP-NLS in the nucleus indicates an assembled nuclear envelope (Anderson et al., 2009). We exclusively imaged female *Drosophila* larvae, which produce four acentric X chromosome fragments upon I-CreI induction (Rong et al., 2002). Control neuroblasts lacking acentrics began accumulating GFP-NLS in telophase when a functional envelope was rebuilt around daughter nuclei (Fig. 1 A). Neuroblasts with acentrics also recruited GFP-NLS around their daughter nuclei at times when acentrics were still segregating poleward (Fig. 1 B). Acentrics (arrows) did not recruit GFP-NLS.

On average, control neuroblasts began accumulating GFP-NLS 216 s (n = 26) after anaphase onset (sister chromatid separation). Neuroblasts with acentrics began accumulating GFP-NLS 252 s (n = 13) after anaphase onset (Fig. 1 C). This 36-s delay, although slight, is significant (P = 0.008 by a two-sided Mann–Whitney–Wilcoxon test) and in accordance with previous studies (Karg et al., 2015; Montembault et al., 2017). Given that initiation of sister acentric separation is delayed by ~200 s (Fig. 1 D), it is unlikely that this delay in nuclear envelope reassembly is sufficient to provide time for incorporation of the acentric. In fact, Fig. 1 D shows that at the time that GFP-NLS begins accumulating in nuclei due to assembled nuclear envelopes, acentrics remain at a significant distance from telophase nuclei. Taken together, these data indicate that additional mechanisms, such as nuclear envelope channels, are required for incorporation of late-segregating acentrics.

Velocity of poleward-segregating acentrics decreases as acentrics pass through nuclear envelope channels

To further understand the mechanism of how acentrics enter telophase daughter nuclei, we live-imaged neuroblasts expressing H2Av-RFP, Lamin-GFP, and I-CreI. As we had previously observed (Karg et al., 2015), we saw that acentrics bypass the physical barrier of the nuclear envelope by entering daughter nuclei through channels in the nuclear envelope (Fig. 1 E, arrowhead).

Before entering nuclei, acentrics first segregate equally to each daughter cell and move poleward through the combined action of protein-coated DNA tethers and bundled microtubules in *Drosophila* neuroblasts (Royou et al., 2010; Karg et al., 2017). Errors in initial poleward segregation often manifest in an unequal partitioning of sister acentrics to each daughter cell (Karg et al., 2017). To explore the functional link between the mechanisms that govern initial acentric segregation and acentric reintegration into daughter nuclei, we determined whether divisions in which acentrics were unequally partitioned had an increased rate of micronuclei formation. However, we found no correlation between unequal acentric segregation and micronuclei formation (Fig. 1 E). Aneuploid daughter cells that received one or three acentrics (arrows) were just as likely to reincorporate their acentrics into daughter nuclei through nuclear envelope channels (73%; n = 11) as euploid daughter cells that received the normal two acentrics (71%; n = 14). This suggests that initial poleward segregation and reintegration into daughter nuclei may be mechanistically uncoupled.

Additionally, we observed that acentrics (arrows) slowed as they passed through nuclear envelope channels (arrowheads)

compared with their poleward movement from the metaphase plate (Fig. 1, F–H). In the division shown in Fig. 1 F (Video 1), the acentric moving toward the bottom nucleus moved at an average of roughly 12 nm/s as it segregated from the metaphase plate to the beginning of the nuclear envelope channel. As the acentric passed through the channel, its velocity decreased to ~4 nm/s. To determine if this slowing is a consistent feature of acentric segregation, we measured the velocity changes in our live imaging of 30 acentrics that reentered daughter nuclei. On average, acentrics began to contact channels ~155 s (n = 30; SD = 48 s) after they began poleward segregation. We deemed the period of acentric movement from their segregation off the metaphase plate to their first contact with nuclear envelope channels as their "initial poleward phase" and the period of acentric movement from when acentrics first contact nuclear envelope channels to when the nuclear envelope has completely surrounded acentrics as their "channel passage phase." We calculated distance by measuring from the furthest tip of the acentric to the nearest point on the daughter nucleus (Fig. 1 G). Overall, we found that acentrics moved through the initial poleward phase with an average velocity of ~10 nm/s (n = 30; SD = 4 nm/s), while they moved through the channel passage phase with an average velocity of ~7 nm/s (n = 30; SD = 4 nm/s; Fig. 1 H). This decrease in acentric velocity while passing through channels was statistically different from acentric velocity during initial poleward segregation as determined by a two-sided Wilcoxon signed-rank test (P = 0.0003). Taken together, these results suggest that acentric poleward segregation before reaching the nuclear envelope and acentric passage through the nuclear envelope involve distinct forces and perhaps distinct mechanisms.

Nuclear envelope channels extend toward acentrics and retract as acentrics rejoin daughter nuclei

Because velocity decreases as acentrics pass through nuclear envelope channels, we hypothesized that the environment of the channel itself may contribute to the observed change in acentric velocity. We therefore imaged neuroblasts expressing I-CreI, H2Av-RFP, and Lamin-GFP and performed a detailed analysis of the dynamics of channels at the time when acentrics passed through them to reenter daughter nuclei (Fig. 2).

Fig. 2 A (Video 2) shows the typical dynamics of nuclear envelope channels as acentrics enter and pass through to rejoin daughter nuclei. As acentrics (arrows) segregated, we observed lamin assembly on the poleward side of daughter nuclei as has been previously reported (Katsani et al., 2008; Warecki and Sullivan, 2018). Nuclear envelope channels (arrowheads) were clearly visible in the lamin as acentrics approached daughter nuclei. We observed lamin extend outwards from channels (brackets) and toward acentrics. Lamin extensions did not completely envelop the acentric but extended only partway along the segregating acentric, leaving the midzone-facing tip of the acentric lamin-free. As the acentrics passed through channels, the lamin extensions retracted toward the daughter nuclei (Fig. 2, A and A′). After this retraction, lamin completed reassembly around the distal tips of the acentrics to ensure that the acentrics and daughter nuclei were completely surrounded by an intact nuclear envelope.
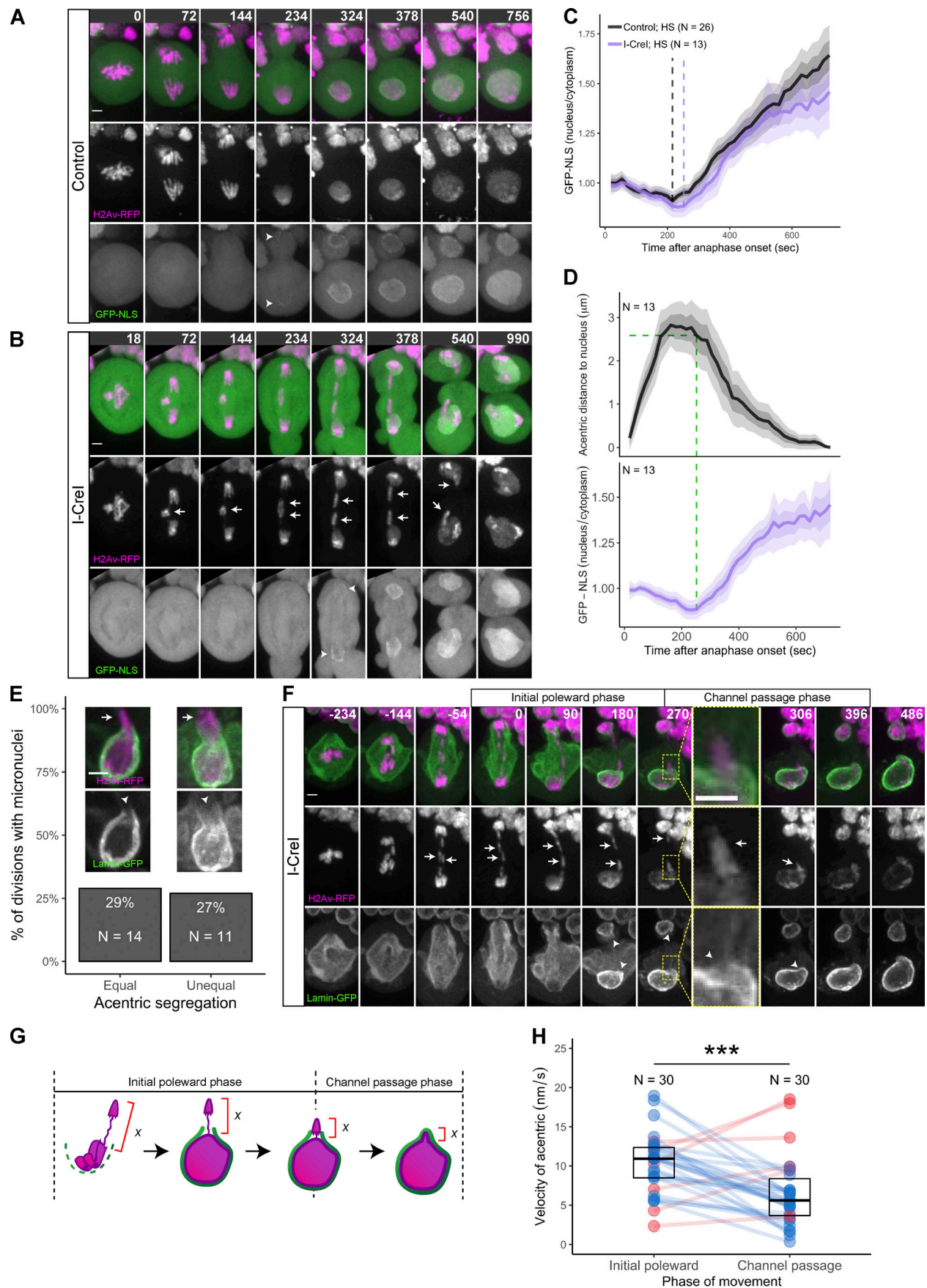
Warecki et al.
ESCRT-III drives chromosome fragments into nuclei

Journal of Cell Biology 4 of 22
https://doi.org/10.1083/jcb.201905091

Figure 1. **Velocities of poleward-segregating acentrics decrease as acentrics pass through nuclear envelope channels. (A and B)** Stills from videos of mitotic neuroblasts expressing H2Av-RFP (magenta) and GFP-NLS (green; A) or H2Av-RFP, GFP-NLS, and I-CreI (B). Nuclear envelope reassembly initiation (arrowheads) began later in the division with late-segregating acentrics (arrows). Despite this delay, the delay in acentric segregation is much more severe, and thus acentrics were still far from the daughter nuclei when the nuclear envelope initiated reassembly. Time is written in seconds after anaphase onset. Scale bars are 2 µm. **(C)** GFP-NLS intensity on daughter nuclei from control neuroblasts (black line; n = 26) and neuroblasts expressing I-CreI (purple line; n = 13). Lines represent averages. Dark-shaded regions represent ± the standard error. Light-shaded regions represent ± twice the standard error. Dashed lines indicate time of nuclear envelope reassembly initiation. On average, nuclear envelope reassembly initiated later in neuroblasts expressing I-CreI (difference in the times of GFP-NLS accumulation on nuclei between control and I-CreI neuroblasts measured as significant by a two-sided Mann–Whitney–Wilcoxon test: P = 0.008). **(D)** Distance of acentrics from control daughter nuclei (black line; n = 13) and GFP-NLS intensity on daughter nuclei from neuroblasts expressing I-CreI (purple line; n = 13). Lines represent averages. Dark-shaded regions represent ± the standard error. Light-shaded regions represent ± twice the standard error. Dashed line indicates the distance of acentrics from daughter nuclei at the time of nuclear envelope reassembly initiation. On average, acentrics were >2.5 µm away from daughter nuclei when the nuclear envelope initiated reassembly. **(E)** Percentage of neuroblast divisions in which acentrics formed micronuclei when segregating equally to each daughter cell (left; n = 14) and when segregating unequally to each daughter cell (right; n = 11). Additionally, stills from videos of mitotic neuroblasts expressing I-CreI, H2Av-RFP (magenta), and Lamin-GFP (green) when acentrics (arrows) segregated equally (left) and unequally (right) and entered daughter nuclei through channels in the nuclear envelope (arrowheads). Scale bar is 2 µm. **(F)** Stills from a video (Video 1) of a mitotic neuroblast expressing I-CreI, H2Av-RFP (magenta), and Lamin-GFP (green). Acentrics (arrows) moved off the metaphase plate and toward daughter nuclei during the initial poleward phase (0–270 s) before entering nuclear envelope channels (arrowheads) and being surrounded by a complete nuclear envelope (270–396 s) during the channel passage phase. Time is written in seconds after initial acentric poleward movement. Scale bar is 2 µm. Yellow dashed boxes indicate magnified regions. **(G)** Diagram illustrating how acentric velocities were measured. The time between when acentrics first move poleward and when they enter nuclear envelope channels is deemed the initial poleward phase. The time between when acentrics first enter channels and when the nuclear envelope reassembles completely around them is termed the channel passage phase. Distance was measured between the furthest point on the acentric and the closest point on the daughter nucleus (red brackets). Velocity was calculated as the difference in measured distances at the beginning and ending of each phase divided by the time it took for acentrics to complete each phase. **(H)** Velocities of acentrics (n = 30) during their initial poleward phase (left) and during their channel passage phase (right). Each dot represents one acentric. Lines connect the measured initial poleward and channel passage velocities of the same acentric. The velocities of 24 of 30 acentrics decreased from their initial poleward phase to their channel passage phase (blue dots). The velocities of 6 of 30 acentrics increased from their initial poleward phase to their channel passage phase (red dots). Boxes represent interquartile ranges and lines represent medians of the measured data. Asterisks indicate statistical significance (P = 0.0003) determined by a two-sided Wilcoxon signed-rank test.

We measured the longest length of the lamin extensions during acentric segregation and the length of the retracted extension at the time of completion of lamin reassembly for all divisions imaged (Fig. 2 B). On average, we found that lamin extended 1.9 µm (n = 18; SD = 0.5 µm) away from daughter nuclei at their longest extension. Upon complete lamin reassembly around the daughter nucleus, extensions were 1.5 µm (n = 18; SD = 0.7 µm) away from daughter nuclei. The retraction of lamin extensions was statically significant, as determined by a paired two-sided t test (P = 0.005). We hypothesized that the observed variation in the lamin extension length might be due to variation in the distance of each acentric from its daughter nucleus. Although one would expect that acentrics farther from nuclei would have channels with longer lamin extensions, we observed only a weak positive correlation (r = 0.23) between the distances of the nearest point on the acentric to the daughter nucleus at the time when channels begin to form and of the longest lamin extension measured (Fig. 2 C). We observed a mild positive correlation (r = 0.32) between the distance the lamin extensions retracted and the distance acentrics traveled during the time of retraction (Fig. 2 D). This suggests that the extension and retraction of the lamin may be mechanistically linked to acentric passage through the channel.

Acentric entry through channels is associated with global disruptions in nuclear morphology

We subsequently determined how the lamin extensions from channels affected the overall morphology of daughter nuclei. We performed lattice light-sheet microscopy on neuroblasts expressing I-CreI, H2Av-RFP, and Lamin-GFP (Fig. 2 E). In this experiment, we observed neuroblasts that divided without

acentrics, neuroblasts that divided with acentrics that entered daughter nuclei through nuclear envelope channels, and neuroblasts that divided with acentrics that formed micronuclei due to a lack of nuclear envelope channels on the daughter nuclei. We focused our attention on the phase when lamin reassembly had just completed encompassing the daughter nucleus. In general, we found that daughter nuclei from divisions with no acentrics were fairly smooth and spherical. In contrast, divisions with acentrics (arrows) that entered daughter nuclei through nuclear envelope channels often exhibited global disruptions in morphology: they were wrinkled and adopted an elongated shape. Surprisingly, we sometimes also observed nuclear envelope protrusions in regions of the daughter nucleus opposite to the acentric entry point (Fig. 2 E, asterisk). Daughter nuclei from divisions with acentrics that formed micronuclei due to a lack of channels exhibited an intermediate morphology and were somewhat elongated but not as wrinkled as nuclei from divisions with acentrics that had entered through channels.

To quantify these observations, we measured the sphericity of each daughter nucleus (Fig. 2 F; also see Materials and methods). Perfect spheres have a sphericity of 1. Daughter nuclei from divisions with no acentrics had an average sphericity of 0.823 (SD = 0.010; n = 6). The average sphericity of daughter nuclei from divisions with acentrics that entered nuclei through channels decreased to 0.731 (SD = 0.059; n = 7), a statistically significant decrease (P = 0.003 by a two-sided Mann–Whitney–Wilcoxon test). Daughter nuclei from divisions with acentrics that formed micronuclei due to the absence of channels had an average sphericity of 0.804 (SD = 0.039; n = 3), with a range of values corresponding to both outcomes. Taken together, these data suggest that lamin reassembly around
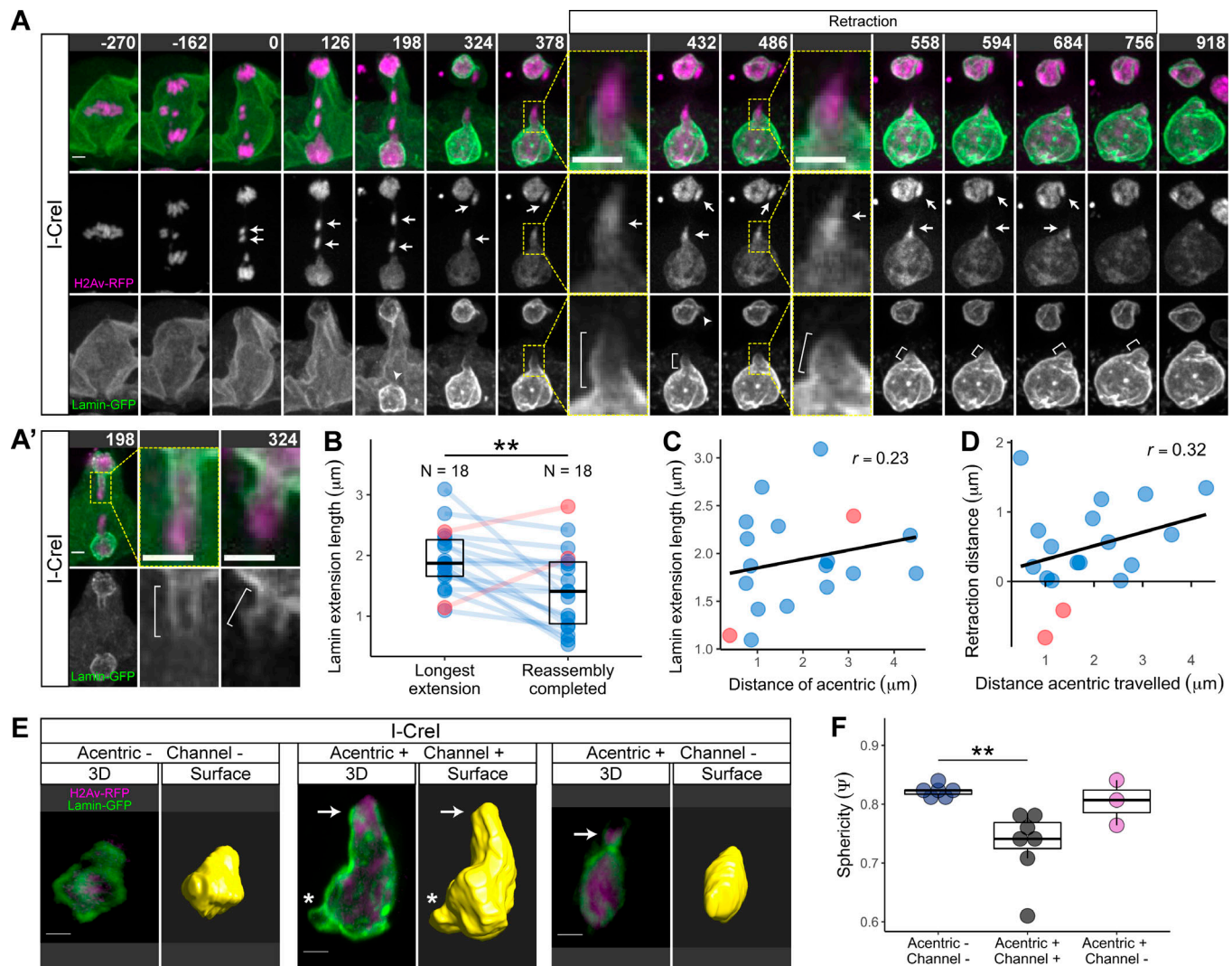
Figure 2. **Lamin extends from nuclear envelope channels and retracts as acentrics rejoin daughter nuclei. (A and A′)** Stills from videos (Video 2) of two mitotic neuroblasts expressing I-CreI, H2Av-RFP (magenta), and Lamin-GFP (green). As acentrics (arrows) approached nuclear envelope channels (arrowheads), lamin extended outward from the channels toward the acentric (brackets). As the acentrics passed through channels to rejoin nuclei, these lamin extensions retracted back. Time is written in seconds after initial acentric poleward movement. Scale bars is 2 µm. Yellow dashed boxes indicate magnified regions. **(B)** Lengths of lamin extensions ($n = 18$) at their longest point during acentric segregation (left) and at the time the nuclear envelope has completed reassembly (right). Each dot represents the length of a lamin extension from one nucleus. Lines connect the extension lengths at their longest value and at completed nuclear envelope reassembly for the same nucleus. The lengths of 16 of 18 lamin extensions decreased from their longest value during acentric segregation to complete nuclear envelope reassembly (blue dots). The lengths of 2 of 18 lamin extensions increased from their longest value during acentric segregation to complete nuclear envelope reassembly (red dots). Boxes represent interquartile ranges and lines represent medians of the measured data. Asterisks indicate statistical significance ($P = 0.005$) determined by a paired two-sided t test. **(C)** Correlation between the distance of the nearest point on the acentric to the nucleus at the time of channel formation (x axis) and to the longest length of the lamin extension during acentric segregation (y axis). Each dot represents one acentric/nucleus pair ($n = 18$). Blue dots represent acentric/nucleus pairs whose lamin extensions decreased by the time of complete nuclear envelope reassembly. Red dots represent acentric/nucleus pairs whose lamin extensions increased by the time of complete nuclear envelope reassembly. The black line is the regression line for all data points. **(D)** Starting at the time of maximum lamin extension, the correlation between the distance an acentric travels (x axis) and the distance the lamin extension retracts during the same time period (y axis). Each dot represents one acentric/nucleus pair ($n = 18$). Blue dots represent acentric/nucleus pairs whose lamin extensions decreased by the time of complete nuclear envelope reassembly. Red dots represent acentric/nucleus pairs whose lamin extensions increased by the time of complete nuclear envelope reassembly. The black line is the regression line for all data points. **(E)** 3D reconstructions from videos of mitotic neuroblasts expressing I-CreI, H2Av-RFP (magenta), and Lamin-GFP (green) imaged on a lattice light-sheet microscope (left). Constructed surface models of the nuclear envelope are shown to the right of each image. Images are representative of I-CreI–expressing neuroblasts that had no acentrics (left), had acentrics and nuclear envelope channels (middle), or had acentrics (arrows) and no channels (right). While divisions with no acentrics and divisions with acentrics but no channels formed smooth daughter nuclei, divisions with acentrics and channels had daughter nuclei that were wrinkled and protruded, including at locations far from where the acentric had entered (asterisk). Scale bars are 2 µm. **(F)** Measurement of the sphericity of the nuclear envelopes of daughter nuclei from neuroblasts expressing I-CreI that had no acentrics (left; $n = 6$), acentrics and channels (middle; $n = 7$), or acentrics but no channels (right; $n = 3$). Divisions with both acentrics and channels had daughter nuclei with relatively lower sphericities than those from divisions with no acentrics and divisions with acentrics but no channels. Boxes represent interquartile ranges and lines represent medians of the measured data. Asterisks indicate statistical significance ($P = 0.003$) by a two-sided Mann–Whitney–Wilcoxon test. The difference between divisions with channels and divisions with micronuclei was not statistically different ($P = 0.07$) as was the difference between divisions without acentrics and divisions with micronuclei ($P = 0.5$), determined by two-sided Mann–Whitney–Wilcoxon tests.

Warecki et al.
ESCRT-III drives chromosome fragments into nuclei

Journal of Cell Biology 6 of 22
https://doi.org/10.1083/jcb.201905091

daughter nuclei is globally altered when nuclear envelope channels form in response to the presence of acentrics.

Late-segregating acentrics are associated with nuclear envelope membrane but not lamina or nuclear pore complexes
We next examined whether the segregating acentrics were associated with certain components of the nuclear envelope and whether the reassembling nuclear envelope mediates acentric reintegration into daughter nuclei. The nuclear envelope consists of the lamina, a double phospholipid bilayer, nuclear pore complexes, and a subset of proteins that are embedded in the inner nuclear membrane, termed INM proteins (Schooley et al., 2012). At the beginning of mitosis, these structures disassemble and remodel as the nuclear envelope breaks down. We and others have shown that while lamin and nuclear pore complexes can reassemble on telophase daughter nuclei, lagging chromatin remains free of these two components (Afonso et al., 2014; Karg et al., 2015; de Castro et al., 2017; Liu et al., 2018). Interestingly, lagging whole chromosomes that form micronuclei recruit a nuclear membrane despite initially lacking lamin or nuclear pore complexes (Liu et al., 2018; de Castro et al., 2017; Maass et al., 2018). However, it is unknown whether lagging acentrics that rejoin daughter nuclei also recruit a nuclear membrane. To explore the behavior of different components of the nuclear envelope during acentric segregation and reintegration into daughter nuclei, we live imaged dividing neuroblasts expressing I-CreI, H2Av-RFP, and either Lamin-GFP or GFP-nucleoporin 107 (Nup107). We also performed superresolution imaging on fixed neuroblasts stained with antibodies recognizing the integral membrane protein Otefin (Fig. 3). Otefin is a member of the LEM (LAP2, Emerin, MAN1) domain family (Barton et al., 2013) that localizes to the INM. Consequently, Otefin localization is used as a nuclear membrane marker (Ashery-Padan et al., 1997).

First, we examined lamina reformation during divisions with acentrics. We monitored lamin dynamics by imaging neuroblasts expressing Lamin-GFP, a ubiquitously expressed lamin orthologous to mammalian Lamin B (Riemer et al., 1995; Fig. 3 A and Video 3). As we had previously found, segregating acentrics (Fig. 3 A, arrows) remained free of Lamin-GFP when daughter nuclei (Fig. 3 A, arrowheads) accumulated Lamin-GFP (Karg et al., 2015). We quantified this observation for all imaged divisions by measuring the fluorescence intensities of the Lamin-GFP signals around both the main nuclei and the acentrics for 342 s (20 time points) from when acentrics began segregating poleward (Fig. S1). We found that Lamin-GFP signal intensity increased around the main nuclei as nuclear envelope reassembly began, but Lamin-GFP signal intensity around acentrics remained relatively low and constant (Fig. 3 A′).

We next monitored nuclear pore complex reassembly when neuroblasts divided with acentrics. The nuclear pore complex is composed of nucleoporins, among which Nup107 is a component of the core Nup107-160 subcomplex (Walther et al., 2003). We monitored nuclear pore complex dynamics by imaging neuroblasts expressing GFP-Nup107 (Fig. 3 B and Video 4). As we observed before (Karg et al., 2015), segregating acentrics (Fig. 3 B, arrows) were mostly free of GFP-Nup107 while daughter nuclei (Fig. 3 B, arrowheads) accumulated GFP-Nup107. We

sometimes detected GFP-Nup107 localizing to acentrics as they neared daughter nuclei, similar to the behavior of lamin extensions we had previously observed. We quantified the fluorescence intensities of the GFP-Nup107 signals on the main nuclei and acentrics for 342 s for all divisions imaged. As we observed with the nuclear lamina, we found that GFP-Nup107 signal intensities increased around the main nuclei when the nuclear envelope began reassembling, while GFP-Nup107 signal intensity around acentrics remained low and constant (Fig. 3 B′).

Next, we fixed neuroblasts, stained using antibodies recognizing the INM protein Otefin, and performed Airyscan superresolution imaging (Fig. 3 C). Otefin is a LEM domain family member (Barton et al., 2013), a core component of the nuclear envelope. Its appearance indicates the presence of nuclear membrane (Ashery-Padan et al., 1997). In neuroblasts fixed in anaphase, we did not observe notable Otefin localization to acentrics (arrows) or to segregating undamaged chromosomes, consistent with the nuclear envelope being broken down at this time. During telophase, we observed Otefin begin to localize to the periphery of daughter nuclei. In addition, we also detected strong Otefin signal on acentrics. Compared with the Otefin signal on daughter nuclei, which was faint and interrupted, we observed bright Otefin staining on acentrics that persisted into late telophase as acentrics entered daughter nuclei. Otefin first localized surrounding the acentric and then as a channel when acentrics began to enter daughter nuclei. Finally, Otefin signal was brightest at the midzone-facing tip of acentrics as the acentrics completed their entry into nuclei. In interphase, we detected a strong Otefin signal around the periphery of daughter nuclei. We were unable to detect any Otefin signal on the tether connecting acentrics to daughter nuclei. We interpret these results as indicating that Otefin and nuclear membrane are enriched on late-segregating acentrics that enter daughter nuclei.

Barrier-to-autointegration factor (BAF) localizes to acentrics, and membrane on acentrics fuses to membrane on daughter nuclei as acentrics pass through channels
In telophase, the ER restructures to provide membrane for the reforming nuclear envelope (Ellenberg et al., 1997). The lumen of the ER is continuous with the perinuclear space between the outer nuclear membrane and the INM, and so marking luminal ER proteins is a strategy to visualize nuclear membrane dynamics (Bobinnec et al., 2003; Bergman et al., 2015; Yao et al., 2018). To further investigate the dynamics of the nuclear membrane on late-segregating acentrics, we live-imaged neuroblasts expressing I-CreI and the luminal ER protein protein disulfide isomerase (PDI) fused to GFP.

In contrast to Lamin-GFP and GFP-Nup107, which were not recruited to late-segregating acentrics, we observed PDI-GFP signals on daughter nuclei and on acentrics (Fig. 4 A, arrows; and Video 5). This was expected given the Otefin localization we observed when we fixed neuroblasts. Late-segregating acentrics first recruited PDI-GFP soon after they moved off the metaphase plate. We quantified the fluorescence intensities of PDI-GFP signals on acentrics and main nuclei for 342 s from when acentrics began poleward movement for all divisions imaged. Unlike with the signal intensities for Lamin-GFP and GFP-Nup107,
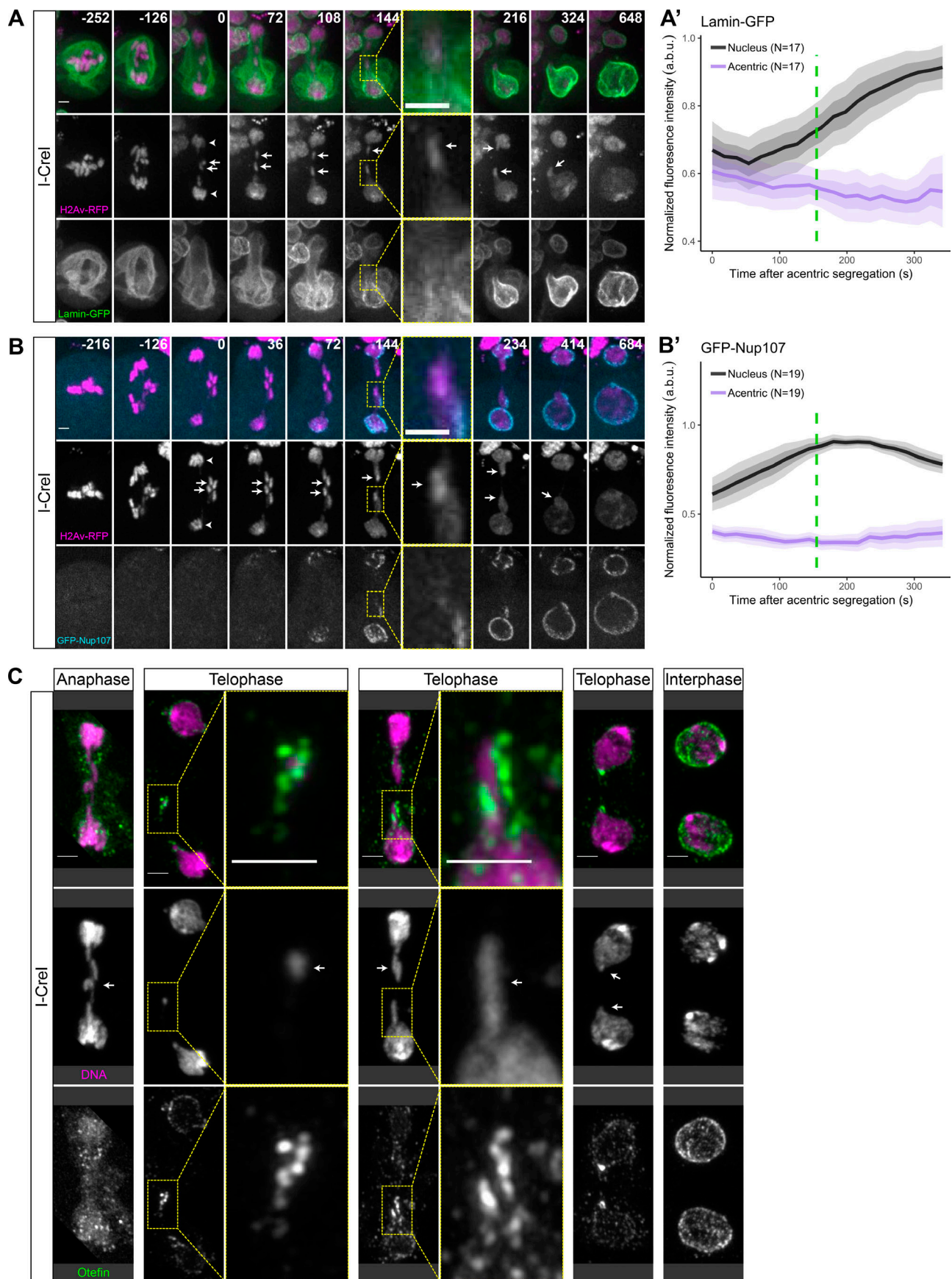
Warecki et al.
ESCRT-III drives chromosome fragments into nuclei

Journal of Cell Biology 7 of 22
https://doi.org/10.1083/jcb.201905091

Figure 3.   **Late-segregating acentrics are associated with nuclear envelope membrane but not lamina or nuclear pore complexes. (A and B)** Stills from videos of mitotic neuroblasts expressing I-CreI and H2Av-RFP (magenta) and either Lamin-GFP (A; Video 3, green) or GFP-Nup107 (B; Video 4, cyan). Daughter nuclei (arrowheads) accumulated Lamin-GFP and GFP-Nup107 during late anaphase/early telophase. However, acentrics (arrows) did not associate with Lamin-GFP and often did not associate with GFP-Nup107. We sometimes observed GFP-Nup107 localize to acentrics near daughter nuclei (Fig. 2 B; 144–234 s). Scale bars are 2 μm. Yellow dashed boxes indicate magnified regions. **(A′ and B′)** Fluorescence intensity of Lamin-GFP (A′; n = 17) or GFP-Nup107 (B′; n = 19) measured on the nuclei (black lines) and the acentrics (purple lines). Lines represent averages. Dark-shaded regions represent ± the standard error. Light-shaded regions represent ± twice the standard error. Dashed green lines represent the previously measured average time when acentrics begin passing through channels (155 s after acentric segregation). Lamin-GFP and GFP-Nup107 fluorescence intensity increased over time as the nuclear envelope reformed on daughter nuclei but remained consistently low on acentrics. See also Fig. S1. a.b.u., arbitrary brightness unit. **(C)** Superresolution images of fixed neuroblasts expressing I-CreI. Neuroblasts were stained with DAPI (magenta) and anti-Otefin antibody (green). In anaphase, Otefin did not strongly localize to acentrics (arrows), and nuclear Otefin staining was sporadic. In contrast, during telophase, Otefin localized around the rim of daughter nuclei and strongly on the acentrics. In interphase, Otefin localized around the rim of nuclei. Scale bars are 2 μm. Yellow dashed boxes indicate magnified regions.

PDI-GFP signal intensity around the main nuclei decreased as cells progressed from anaphase to telophase (Fig. 4 A′). Presumably, the observed decrease in PDI-GFP signal intensity around main nuclei was due to the fluorophore photobleaching, as it has been well established that nuclear membrane is recruited to reforming nuclei (Chaudhary and Courvalin, 1993; Ellenberg et al., 1997). In contrast to the Lamin-GFP and GFP-Nup107 signal intensities on segregating acentrics, which were lower than those on the main nuclei and remained constant while signal intensity around the main nuclei increased, we found that PDI-GFP signal intensity around acentrics was higher than that of main nuclei and stayed constant while the signal intensity around the main nuclei decreased (Fig. 4 A′). Given the observed decrease in PDI-GFP signal intensity on the main nuclei during the time period of nuclear envelope reassembly, we interpret the high, constant PDI-GFP signal intensity on acentrics as indicative of strong PDI-GFP recruitment to acentrics.

We observed acentrics reenter daughter nuclei through highly localized gaps in all three major components of the nuclear envelope surrounding daughter nuclei, including in the PDI-GFP signal (Fig. 4 B, arrows). While the main nuclei were almost completely coated with a layer of PDI-GFP, the acentrics exhibited highly variable association with PDI-GFP, with some acentrics almost completely surrounded by PDI-GFP while others had only one or two sides coated (compare acentrics in Fig. 4, A–C). In addition, the PDI-GFP signal associated with acentrics was dynamic and could dissociate and reassociate with acentrics as they moved toward daughter nuclei (Fig. 4 C). As acentrics began to pass through the channels formed in the nuclear membrane around main nuclei, we observed the PDI-GFP signal on acentrics (Fig. 4 C, top arrow) and the PDI-GFP signal on main nuclei (Fig. 4 C, bottom arrow) merge (Fig. 4 C, asterisk). Taken together, these results suggest that late-segregating acentrics rejoining daughter nuclei recruit a nuclear membrane that fuses with the membrane on the daughter nuclei as acentrics pass through channels in the nuclear envelope to rejoin undamaged chromosomes.

Because we observed both nuclear membrane and the LEM-domain protein Otefin enrich on late-segregating acentrics, we hypothesized that there might be factors specifically recruiting them to acentrics. A good candidate protein is BAF. BAF cross-bridges DNA during mitosis with undamaged chromosomes to ensure the nuclear envelope surrounds all chromosomes in a single nucleus (Samwer et al., 2017). BAF recruits LEM-domain proteins to telophase chromatin

(Shumaker et al., 2001; Haraguchi et al., 2001). In addition, BAF localizes at and recruits LEM-domain proteins and membrane to the sites of nuclear envelope rupture in interphase cells to stimulate repair (Halfmann et al., 2019).

To test if BAF localizes to acentrics, we live-imaged neuroblasts expressing H2Av-RFP, GFP-BAF, and I-CreI (Fig. 4 D). We observed GFP-BAF localizing to both daughter nuclei (Fig. 4 D, arrowheads) and acentrics (Fig. 4 D, arrows) during telophase. At first, GFP-BAF accumulated equally to acentrics and daughter nuclei. However, later in telophase, GFP-BAF accumulation was much stronger on acentrics than on daughter nuclei. As with Otefin, we observed GFP-BAF initially localize all around acentrics and then concentrate at the midzone-facing tips of acentrics as they completed their entry into daughter nuclei. Additionally, we observed GFP-BAF localizing to the tethers that connect acentrics to daughter nuclei. We also detected GFP-BAF along threads that apparently connect acentrics segregating to opposing daughter cells. In interphase, we observed even GFP-BAF localization around the entire daughter nucleus.

We quantified this observation for all imaged divisions (Fig. S1) and found that GFP-BAF signal intensity increased at the same rate around the main nuclei and acentrics as nuclear envelope reassembly began (Fig. 4 D′). Then, GFP-BAF intensity dramatically increased on acentrics around the time that acentrics begin entering nuclear envelope channels. These results indicate that BAF is enriched on late-segregating acentrics that enter daughter nuclei. Enriched BAF on acentrics might recruit LEM-domain proteins, such as Otefin, and nuclear membrane, analogous to repair of nuclear envelope ruptures in interphase cells (Halfmann et al., 2019).

Membrane fusion protein Comt/NSF and ESCRT-III components Shrub/CHMP4B and CHMP2B are required for efficient acentric reintegration into daughter nuclei

Because of the apparent fusion between nuclear membrane on late-segregating acentrics and nuclear membrane surrounding main nuclei as acentrics pass through nuclear envelope channels, we hypothesized that membrane fusion genes may play an important role in acentric reintegration into daughter nuclei. The time required for fusion events between membrane on acentrics and membrane on nuclei may also explain the marked decrease in the velocity of acentrics as they pass through nuclear envelope channels. During nuclear envelope reassembly in divisions lacking lagging chromatin, the ER restructures to extend membrane
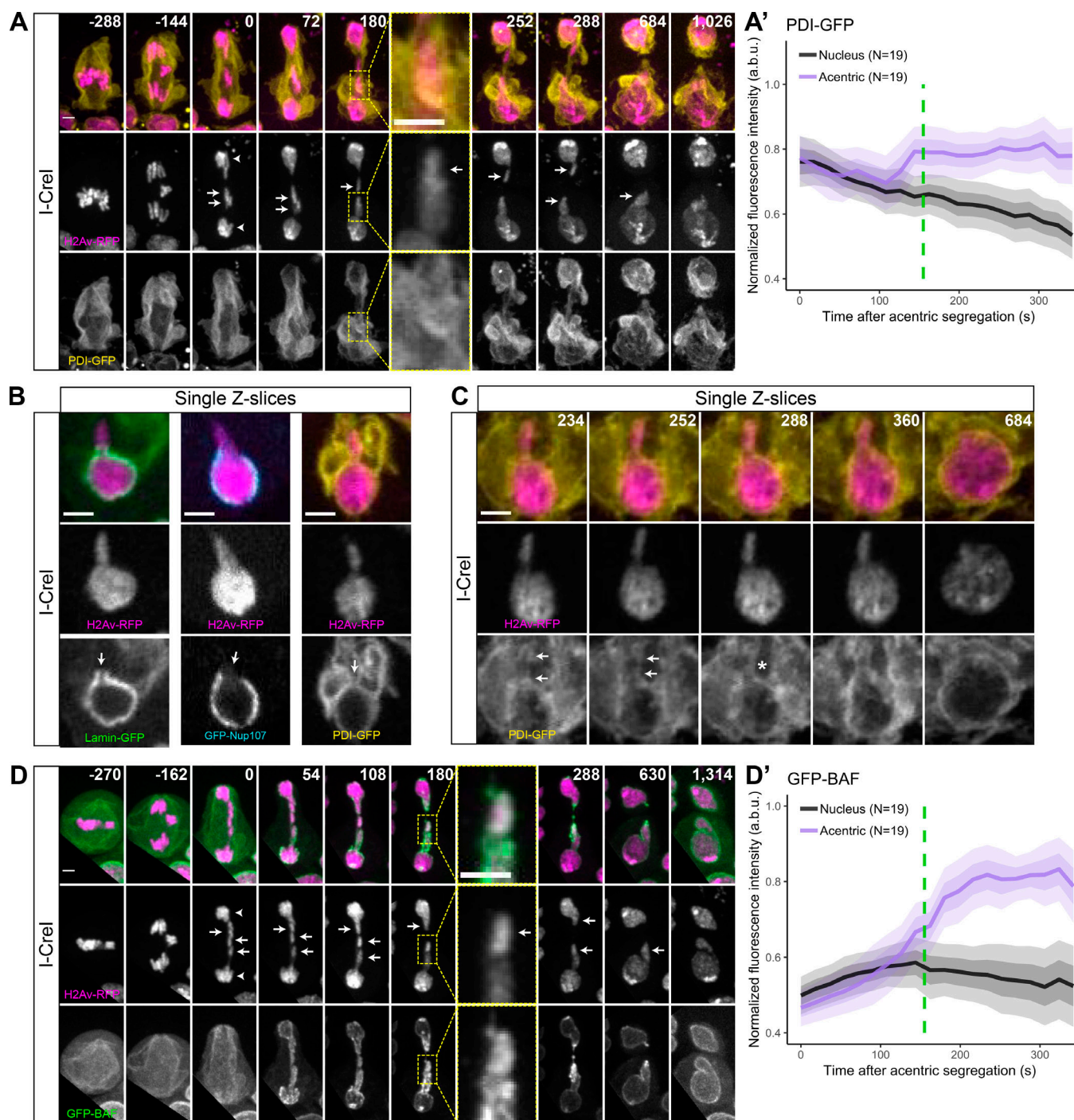
Figure 4. **BAF is enriched on late-segregating acentrics, and membrane between acentrics and daughter nuclei fuses. (A)** Stills from a video of a mitotic neuroblast expressing I-CreI, H2Av-RFP (magenta), and PDI-GFP (Video 5; yellow). Scale bars are 2 µm. Yellow dashed boxes indicate magnified regions. **(A′)** Fluorescence intensity of PDI-GFP measured on the nuclei (black line; n = 19) and on the acentrics (purple line; n = 19). Lines represent averages. Dark-shaded regions represent ± the standard error. Light-shaded regions represent ± twice the standard error. Dashed green lines represent the previously measured average time when acentrics began passing through channels (155 s after acentric segregation). PDI-GFP fluorescence became much stronger on acentrics than on daughter nuclei as cells progressed through anaphase to telophase. See also Fig. S1. a.b.u., arbitrary brightness unit. **(B)** Stills from videos of mitotic neuroblasts expressing I-CreI, H2Av-RFP, and Lamin-GFP (left), GFP-Nup107 (middle), or PDI-GFP (right). Each image is a single Z-slice of one daughter nucleus. Channels in the nuclear envelope (arrows) formed in all three major components of the nuclear envelope, allowing acentrics to enter daughter nuclei. Scale bars are 2 µm. **(C)** Stills from a video of a mitotic neuroblast expressing I-CreI, H2Av-RFP, and PDI-GFP. As the acentric approached the daughter nucleus, nuclear membrane on the acentric and daughter nucleus (arrows) fused (asterisk). Time is written in seconds after initial acentric poleward movement. Each image is a single Z-slice. Scale bar is 2 µm. **(D)** Stills from a video of a mitotic neuroblast expressing I-CreI, H2Av-RFP (magenta), and GFP-BAF (green). During telophase, BAF accumulated at the nuclear rim of daughter nuclei and strongly on the late-segregating acentrics (arrows). Time is written in seconds after acentric segregation. Scale bars are 2 µm. Yellow dashed boxes indicate magnified regions. **(D′)** GFP-BAF intensity on daughter nuclei (black line; n = 19) and acentrics (purple line; n = 19). Lines represent averages. Dark-shaded regions represent ± the standard error. Light-shaded regions represent ± twice the

Warecki et al.
ESCRT-III drives chromosome fragments into nuclei

Journal of Cell Biology
https://doi.org/10.1083/jcb.201905091

10 of 22

standard error. Dashed line represents the average time that acentrics enter nuclear envelope channels (155 s). GFP-BAF is recruited to both daughter nuclei and acentrics as neuroblasts enter telophase. At around the time when acentrics first begin to enter nuclear envelope channels, GFP-BAF is dramatically enriched on acentrics.

that first contacts and then spreads over decondensing chromatin to form the nuclear membrane (Ellenberg at al., 1997). Canonical membrane fusion genes, including NSF and SNARE proteins, mediate fusion of distinct nuclear membrane sections to form a continuous membrane sheet around daughter nuclei (Baur et al., 2007). Nuclear membrane fusion also requires the ESCRT-III complex (Vietri et al., 2015; Olmos et al., 2015). We hypothesized that membrane fusion events between nuclear membrane on acentrics and nuclear membrane on the main nuclei would require a similar set of proteins.

To determine if membrane fusion is required for efficient acentric reintegration into daughter nuclei, we performed a candidate-based RNAi screen where we depleted single membrane fusion proteins and used live imaging to monitor if the rate of acentrics forming micronuclei increased compared with control divisions. We also included several proteins involved in ER organization and function in our screen. In total, we depleted 13 different proteins. We classified acentrics as forming micronuclei if they visibly failed to rejoin daughter nuclei, either as existing physically separate from daughter nuclei or moving separately from daughter nuclei and in a different condensation state. We considered hits from this screen to be proteins that, when knocked down, resulted in a greater than twofold increase in the measured rate of micronuclei formation for control divisions. The results of this screen are summarized in Table 1. In control divisions, acentrics segregated equally in 89% of divisions (n = 27). We observed acentrics forming micronuclei in only ~17% (n = 24) of control divisions. Fig. 5 A (Video 6) shows a typical control division in which the acentrics (arrows) successfully rejoined daughter nuclei. Of note, we observed significant increases in the rate of acentrics forming micronuclei when the levels of Comt/NSF (46%), reticulon 2 (Rtnl2/RTN2; 53%), or Shrub/CHMP4B (51%) were decreased with RNAi compared with control divisions (Table 1).

Fig. 5 B (Video 7) shows a typical Comt-depleted neuroblast division in which an acentric (arrows) formed a micronucleus (arrowhead). Comt is one of two Drosophila homologues of NSF, a protein that disassembles trans-SNARE complexes and allows repeated cycles of membrane fusion (Ordway et al., 1994). In Comt-depleted neuroblasts, sister acentrics were equally segregated in 89% (n = 44) of divisions imaged (compare to control divisions: 89%), suggesting that Comt depletion may not affect the initial poleward segregation of acentrics. However, RNAi depletion of Comt resulted in a dramatic increase in acentrics failing to reintegrate into daughter nuclei, leading to the formation of micronuclei (micronuclei formed in 46% of divisions, n = 46; compared with 17% of control divisions). We confirmed this result by using a second RNAi line against Comt and again observed a high rate of micronuclei formation (43%, n = 40; control, 17%). Additionally, we used the well-characterized comt6 temperature-sensitive mutant (Krishnan et al., 1996; Sanyal and Krishnan, 2012) and likewise observed acentrics

form micronuclei at a high rate in heat shocked comt6/+ heterozygotes (62%, n = 13; control, 17%; Table 1).

Fig. 5 C (Video 8) shows a typical Rtnl2-depleted neuroblast division in which an acentric (arrows) formed a micronucleus (arrowhead). Rtnl2 is likely the Drosophila orthologue of human RTN2 (Thurmond et al., 2019), a reticulon-family protein involved in the restructuring of the ER (Voeltz et al., 2006; Montenegro et al., 2012). In Rtnl2-depleted neuroblasts, acentrics were also equally segregated 89% (n = 35) of the time (compared with 89% of control divisions), indicating that Rtnl2 is not involved in initial acentric segregation. However, upon RNAi-depletion of Rtnl2, acentrics failed to enter daughter nuclei and instead formed micronuclei in 53% (n = 32) of divisions filmed (compared with 17% control divisions).

Fig. 5 D (Video 9) shows a typical Shrub-depleted neuroblast division in which an acentric (arrows) formed a micronucleus (arrowhead). Shrub is the Drosophila orthologue of CHMP4B, a major component of the ESCRT-III complex (Sweeney et al., 2006). In Shrub-depleted neuroblasts, we observed decreased

Table 1. **Summary of results from candidate-based RNAi screen for genes involved in acentric reintegration into daughter nuclei**

Genotype	Stock number	Micronuclei % (N)	Equal segregation % (N)
y1v1	1509	17 (24)	89 (27)
Rtnl2 RNAi	58208	53 (32)	89 (35)
Shrub RNAi	38305	51 (37)	69 (32)
Comt RNAi	31666	46 (46)	89 (44)
Comt RNAi	31470	43 (40)	73 (40)
comt6/+	26708	62 (13)	64 (11)
CHMP2B RNAi	28531	44 (18)	50 (16)
Snap24 RNAi	28719	38 (8)	83 (6)
Membrin RNAi	50515	33 (12)	86 (7)
Snap RNAi	29587	33 (18)	56 (18)
Spastin RNAi	53331	33 (24)	70 (20)
Atlastin RNAi	36736	33 (18)	75 (20)
Usnp RNAi	25862	31 (16)	67 (9)
Rtnl1/+	12425	31 (13)	75 (8)
Syb RNAi	38234	27 (20)	80 (20)
Snap 25 RNAi	34377	23 (13)	67 (9)

Micronucleation and equal segregation rates for lines used in the candidate-based RNAi screen for genes involved in acentric entry into daughter nuclei. Stock numbers are based off the BDSC. Mutant lines (comt6 and Rtnl1) were screened as heterozygotes (+ indicates wild-type chromosome). All other lines expressed RNAi against the indicated gene product. See also Fig. 5.
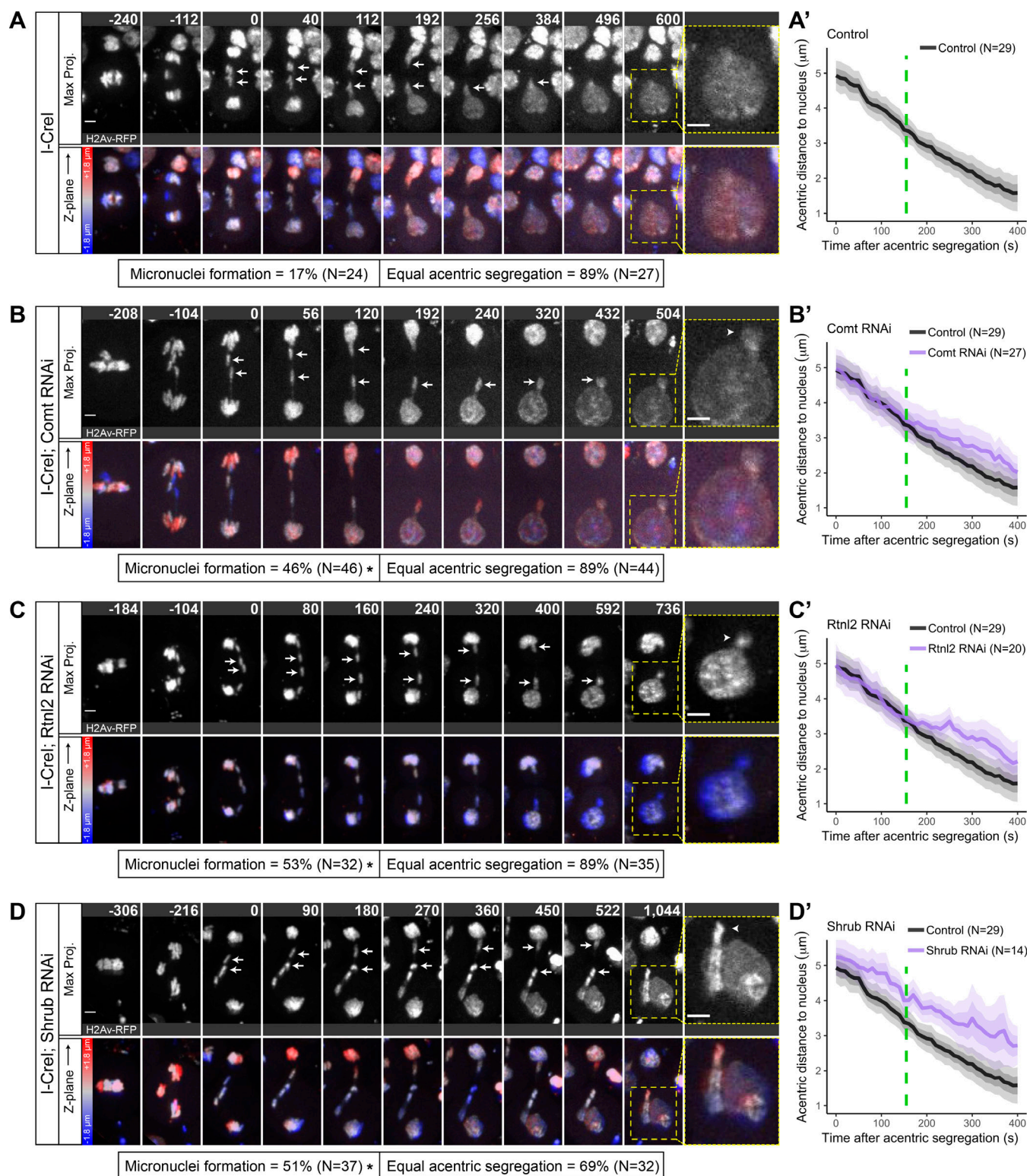
Figure 5. **Comt/NSF, Rtnl2/RTN2, and Shrub/CHMP4B are required for efficient acentric reintegration into daughter nuclei. (A–D)** Stills from videos of mitotic neuroblasts expressing I-CreI and H2Av-RFP (gray) only (A; Video 6), or expressing I-CreI and H2Av-RFP in combination with RNAi against Comt (B; Video 7), Rtnl2 (C; Video 8), or Shrub (D; Video 9). Each panel is composed of a row of maximum projections (top row) above their corresponding sum projections that are pseudo-colored to illustrate differences in Z-position (bottom row; red, upper Z-planes; blue, lower Z-planes). Acentrics (arrows) seg-regated poleward and reentered daughter nuclei in control videos. However, acentrics in dividing neuroblasts expressing RNAi against Comt, Rtnl2, or Shrub initially segregated but failed to reintegrate into daughter nuclei and instead formed micronuclei (arrowheads). Time is written in seconds after initial acentric poleward movement. Scale bars are 2 µm. Yellow dashed boxes indicate magnified regions. Asterisks indicate statistical significance to control as determined by γ^2 tests (B; P = 0.016; C, P = 0.005; D, P = 0.006). **(A'–D')** Distance of acentrics from main nuclei in control (A'–D'; black line; n = 29), Comt-depleted

(B′; purple line; *n* = 27), Rtnl2-depleted (C′; purple line; *n* = 20), and Shrub-depleted (D′; purple line; *n* = 14) neuroblasts. Lines represent averages. Dark-shaded regions represent ± the standard error. Light-shaded regions represent ± twice the standard error. Dashed green lines represent the previously measured average time when acentrics begin passing through channels (155 s after acentric segregation). Although initially following a similar trajectory as acentrics in control neuroblasts, acentrics in both Comt- and Rtnl2-depleted neuroblasts ultimately remained farther apart from daughter nuclei at 400 s after initial acentric segregation than those in control divisions. The point of divergence was approximately the measured time when acentrics begin passing through channels. In contrast, the trajectory of acentrics in Shrub-depleted neuroblasts, which likewise remained farther apart from daughter nuclei at 400 s after initial acentric segregation than those in control divisions, diverged from acentrics in control neuroblasts soon after initial acentric segregation. See also Fig. S3.

---

equal acentric segregation (69%; *n* = 32) compared with controls (89%), suggesting that Shrub may be involved in the initial segregation of acentrics. RNAi depletion of Shrub also resulted in acentrics forming micronuclei in 51% (*n* = 37) of divisions imaged (compared with 17% of control divisions). However, equivalent high rates of micronuclei formation were observed in divisions in which acentrics were partitioned equally (10 of 18) and in which acentrics were partitioned unequally (five of nine). This suggests that the increased rate of micronuclei formation was not due to any defect in initial acentric poleward segregation. We additionally observed a high rate of micronuclei formation (44%; *n* = 18) in divisions when another ESCRT-III component, CHMP2B, was depleted with RNAi.

We next determined whether the increased micronucleation observed upon depletion of Comt, Rtnl2, and Shrub was due to differences in the initial distances of acentrics from daughter nuclei or differences in timing of acentric segregation (Fig. S2). While acentrics in Shrub-depleted neuroblasts were initially slightly farther from daughter nuclei, we found no statistically significant differences in the initial distances of acentrics from daughter nuclei between control neuroblasts and Comt-depleted (P = 0.9), Rtnl2-depleted (P = 0.7), or Shrub-depleted neuroblasts (P = 0.3; Fig. S2 A), as determined by two-sided Mann–Whitney–Wilcoxon tests. Moreover, for each condition, acentrics that formed micronuclei were not initially farther away from daughter nuclei than acentrics that entered nuclei. We also found no statistically significant differences in the time from anaphase onset to acentric segregation between all the conditions (Comt RNAi, P = 0.3; Rtnl2 RNAi, P = 0.07; Shrub RNAi, P = 0.6) as determined by independent two-sided *t* tests, although acentrics from Rtnl2-depleted divisions segregated slightly later than controls (Fig. S2 B). In general, we observed no definitive correlation that linked the time between anaphase onset and acentric segregation to the ability of an acentric to enter the nucleus. Table 2 summarizes these data. Taken together, these results indicate that the increased micronucleation we observed upon RNAi depletion of Comt, Rtnl2, and Shrub was not due to defective initial behavior of segregating acentrics.

To more thoroughly understand when acentric reintegration was affected in Comt-, Rtnl2-, and Shrub-depleted neuroblasts, we measured the distance of the lagging end of the acentric to the nearest point on the main nucleus every 10 s for 400 s after acentrics began their initial poleward movement for an additional set of control and Comt-, Rtnl2-, and Shrub-depleted divisions (Fig. 5, A′–D′). We then compared the trajectory of acentrics in Comt-, Rtnl2-, and Shrub-depleted divisions to the trajectory of acentrics in control divisions (Fig. 5, A′–D′, black line). We reasoned that acentrics failing to enter daughter nuclei should exhibit a measurable increase in distance from main

nuclei than those that reenter nuclei (Fig. S3). In Comt-depleted divisions, the trajectory of acentrics (Fig. 5 B′, purple line) initially matched the trajectory of acentrics from control divisions. However, at the time when acentrics in control divisions begin to enter into nuclear envelope channels (previously measured at 155 s after acentrics began their poleward movement, dashed green line), acentrics from Comt-depleted neuroblasts began to become measurably farther away from daughter nuclei. This pattern was also seen for acentrics from Rtnl2-depleted divisions (Fig. 5 C′, purple line): acentrics from Rtnl2-depleted neuroblasts closely matched the trajectory of acentrics from control divisions until the point when acentrics from control divisions enter channels (155 s, dashed green line), at which point acentrics from Rtnl2-depleted neuroblasts began to become measurably farther away from daughter nuclei. Interestingly, acentrics from Shrub-depleted neuroblasts (Fig. 5 D′, purple line) exhibited a distinct trajectory even during the initial segregation stages. However, after the point when acentrics from control divisions enter channels (155 s; dashed green line), the trajectory of acentrics from Shrub-depleted neuroblasts became even farther away from the trajectory of control acentrics than during the initial segregation period.

Taken together, these results indicate that Comt, Rtnl2, and Shrub are required for efficient acentric entry during the final stage of acentric integration, suggesting that nuclear membrane fusion and ER restructuring events are important mechanisms that ensure late-segregating acentrics pass through nuclear envelope channels.

Failed acentric entry into nuclei in Comt-depleted neuroblasts is not due to gross structural or functional defects in the nuclei

Comt/NSF and ESCRT-III are required to seal nuclear membrane domains during mitosis with undamaged chromosomes (Baur et al., 2007; Vietri et al., 2015; Olmos et al., 2015). To investigate if the failure of acentrics to enter daughter nuclei when Comt, Shrub, and CHMP2B are depleted is due to an inability to properly seal nuclear membranes, we examined if micronucleus formation was correlated with deficient nuclear envelope reassembly.

We live-imaged neuroblasts expressing H2Av-RFP, GFP-NLS, and I-CreI with and without RNAi depletion of Comt (Fig. S4). In control divisions with wild-type levels of Comt (Fig. S4 A), we observed GFP-NLS accumulation to daughter nuclei (arrowheads) soon after acentrics (arrows) began segregating poleward. As telophase progressed, GFP-NLS signal grew brighter on nuclei, indicating membrane sealing. Segregating acentrics did not accumulate GFP-NLS. Acentrics entered daughter nuclei. In divisions with depleted Comt (Fig. S4 B), we also observed GFP-NLS

Table 2. Key characteristics of hits from the candidate-based RNAi screen

Genotype	Stock number	Micronuclei % (N)	Equal segregation % (N)	Distance of acentric to nucleus (µm)	Time of acentric segregation (s)
y1v1	1509	17 (24)	89 (27)	3.6 (SD = 1.5; N = 15)	200 (SD = 60; N = 7)
Comt RNAi	31666	46 (46)	89 (44)	3.5 (SD = 1.2; N = 32)	180 (SD = 50; N = 12)
Rtnl2 RNAi	58208	53 (32)	89 (35)	3.2 (SD = 1.2; N = 23)	300 (SD = 110; N = 7)
Shrub RNAi	38305	51 (37)	69 (32)	3.8 (SD = 0.7; N = 19)	225 (SD = 88; N = 13)

Micronucleation and equal segregation rates, the average distance of acentrics from daughter nuclei at the time of acentric segregation, and the time from anaphase onset to acentric segregation are shown for each hit from our screen. See also Fig. 5.

accumulate on daughter nuclei (arrowheads) soon after acentrics (arrows) began segregating poleward. Segregating acentrics did not accumulate GFP-NLS. Acentrics failed to enter daughter nuclei, forming micronuclei (Fig. S4 B, arrowheads) instead. One of the micronuclei accumulated GFP-NLS while the other did not, representative of a variable capacity of micronuclei to recruit GFP-NLS that we observed throughout this experiment.

We quantified GFP-NLS accumulation on daughter nuclei for all divisions imaged for 40 time points after acentric segregation (Fig. S4, C and C′). GFP-NLS accumulation rates were similar between divisions with and without Comt depletion (Fig. S4 C). We next asked if nuclei from Comt-depleted neuroblasts in which acentrics had formed micronuclei had more difficulty in accumulating GFP-NLS than those from Comt-depleted neuroblasts in which acentrics had reentered daughter nuclei (Fig. S4 C′). We measured a noticeable deficiency in GFP-NLS accumulation when acentrics formed micronuclei. However, this difference was not statistically significant as determined by a Scheirer–Ray–Hare test (P = 0.17). Taken together, these results suggest that the inability of acentrics to enter daughter nuclei when Comt is depleted is not due to gross structural or functional defects in the daughter nuclei. However, Comt depletion may be correlated with defective nuclear membrane sealing, although this is far from clear based on our current analysis.

Shrub/CHMP4B localizes to acentrics as they reintegrate into daughter nuclei

To determine the role of Shrub/CHMP4B in acentric reintegration into daughter nuclei, we analyzed the location of Shrub in neuroblasts dividing with acentrics. We reasoned that if Shrub were involved in acentric reintegration, we would observe Shrub localize to acentrics beginning to contact daughter nuclei. Therefore, we performed live imaging on neuroblasts expressing I-CreI, H2Av-RFP, and Shrub-GFP and quantified when Shrub-GFP localized to acentrics and daughter nuclei (Fig. 6).

Fig. 6 A (Video 10) shows the typical pattern of Shrub-GFP localization during the division of a neuroblast with acentrics. At the time when the acentrics began their initial poleward movement, Shrub-GFP did not localize to either the acentrics (Fig. 6 A, arrows) or the daughter nuclei (Fig. 6 A, arrowheads). In contrast, at the time when the acentrics began to rejoin daughter nuclei, Shrub-GFP puncta (Fig. 6 A, arrowheads) localized both to acentrics and strongly to daughter nuclei. We defined Shrub-GFP puncta as bright spots of fluorescence. Shrub-GFP

puncta localized along the periphery of daughter nuclei, presumably mediating fusion of nuclear membrane on daughter nuclei as previously described (Vietri et al., 2015; Olmos et al., 2015). Shrub-GFP puncta localized to the main body of the acentric and also specifically at the point where the acentric contacted the daughter nucleus before reintegration (Fig. 6 A, 180 s, arrowhead).

We quantified the amount of Shrub-GFP puncta localized to acentrics and daughter nuclei for all divisions imaged (Fig. 6 B). We observed very low Shrub-GFP localization on acentrics (Fig. 6 B, purple line) and on nuclei (Fig. 6 B, black line) in the time period between 90 s before and 90 s after acentrics began their poleward movement. During this time period, only 2 of 15 acentrics were associated with more than one Shrub-GFP punctum at any given time, and 6 of 15 acentrics were associated with Shrub-GFP puncta at consecutive time points. Similarly, only 4 of 15 daughter nuclei were associated with more than one Shrub-GFP punctum at any given time, and 8 of 15 daughter nuclei were associated with Shrub-GFP puncta at consecutive time points. The average number of GFP-puncta on acentrics and daughter nuclei at the time when acentrics began moving poleward was 0 (n = 15; SD = 0) and 0.33 (n = 15; SD = 0.47), respectively.

In contrast, we observed increased Shrub-GFP localization to both acentrics and daughter nuclei in the time period between 90 s before and 90 s after acentrics first contacted daughter nuclei. During this time period, 11 of 14 acentrics were associated with more than one Shrub-GFP punctum at any given time, and 12 of 14 acentrics were associated with Shrub-GFP puncta at consecutive time points. Likewise, 14 of 14 daughter nuclei were associated with more than one Shrub-GFP punctum at any given time, and 14 of 14 daughter nuclei were associated with Shrub-GFP puncta at consecutive time points. The average number of Shrub-GFP puncta on acentrics and daughter nuclei at the time when acentrics contacted daughter nuclei was 0.86 (n = 14; SD = 0.76) and 4.08 (n = 1.75; SD = 1.75), respectively. The average number of Shrub-GFP puncta on acentrics was highest 72 s after acentrics contacted daughter nuclei (1.64; n = 14; SD = 1.17). The average number of Shrub-GFP puncta on daughter nuclei was highest 54 s after acentrics contacted daughter nuclei (4.54; n = 14; SD = 2.37).

Taken together, these results indicate that Shrub/CHMP4B localizes to reintegrating acentrics. Therefore, Shrub/CHMP4B is in the correct place at the correct time to mediate the fusion
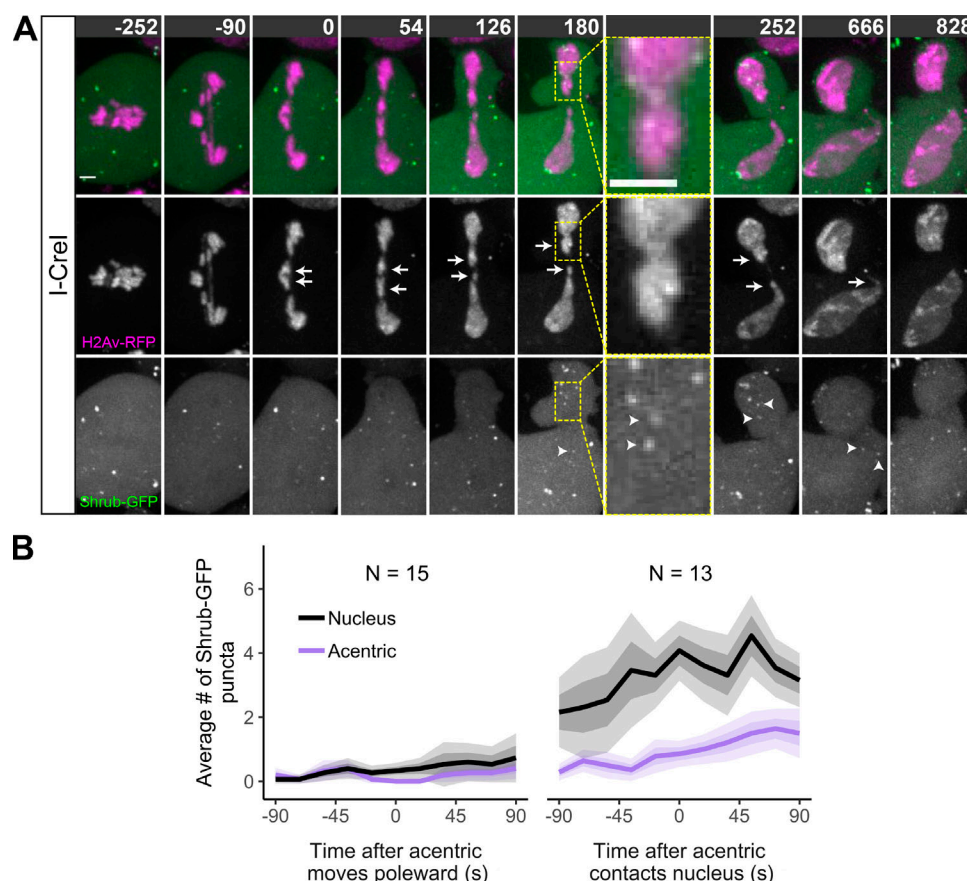
Figure 6. **Shrub/CHMP4B localizes to acentrics as they reintegrate into daughter nuclei. (A)** Stills from a video (Video 10) of a mitotic neuroblast expressing I-CreI, H2Av-RFP (magenta), and Shrub-GFP (green). At the time when acentrics began their initial poleward movement, neither acentrics (arrows) nor daughter nuclei were associated with any Shrub-GFP puncta. When acentrics began to rejoin daughter nuclei, Shrub-GFP puncta localized to both acentrics and daughter nuclei (arrowheads), including to the location where the acentric is contacting the daughter nucleus. Time is written in seconds after initial acentric poleward movement. Scale bars are 2 μm. Yellow dashed boxes indicate magnified regions. **(B)** Average number of Shrub-GFP puncta that localized to acentrics (purple line) and to nuclei (black line) when acentrics initially segregated poleward (left; $n = 15$) and when acentrics rejoined daughter nuclei (right; $n = 13$). For 90 s before and after when acentrics initially segregated poleward, little to no Shrub-GFP puncta localized to acentrics or nuclei. For 90 s before and after acentrics began to contact and reintegrate into nuclei, Shrub-GFP puncta frequently localized to acentrics and to daughter nuclei. Lines represent averages. Dark-shaded regions represent ± the standard error. Light-shaded regions represent ± twice the standard error.

between membrane on acentrics and membrane on daughter nuclei that allows acentric reintegration into daughter nuclei.

Discussion

Chromosome fragments enter telophase nuclei through channels that lack all major components of the nuclear envelope

Cells dividing with lagging whole or broken chromosomes risk losing or damaging a significant part of their genome if these wayward chromosomes are not included in daughter nuclei (Zhang et al., 2015; Ly et al., 2017). While lagging chromosomes are rare in healthy cells due to the evolution of safeguards such as the spindle assembly checkpoint (Sacristan and Kops, 2015) and the DNA damage response (Mikhailov et al., 2002), they are much more frequent in cancer cells, in which these safeguards are often compromised (Thompson and Compton, 2008). For example, colorectal cancer cells frequently bypass these checkpoints to divide with lagging chromosomes (Stewénius et al., 2005; Green

and Kaplan, 2003). Intriguingly, not every lagging chromosome forms a micronucleus: some reincorporate into daughter nuclei to maintain euploidy (Huang et al., 2012; Pidoux et al., 2000; Sabatinos et al., 2015; Liang et al., 1993; Carlson, 1938; Royou et al., 2010; Bretscher and Fox, 2016).

In spite of the fact that incorporation of late-segregating chromosomes and chromosome fragments into daughter nuclei has been documented in multiple systems, the mechanisms that facilitate entry remain elusive. Broken chromosome segregation is often delayed to the point that nuclear envelope reassembly has begun on daughter nuclei before acentrics have rejoined (Fig. 1). Previous work has established that late-segregating acentric fragments remain connected to daughter nuclei through DNA tethers in *Drosophila* neuroblasts (Royou et al., 2010). We have previously observed acentrics enter daughter telophase nuclei by passing through highly localized channels in the layers of lamin and nuclear pore complexes that assemble around daughter nuclei (Karg et al., 2015). We have now additionally demonstrated that channels form in the nuclear

membrane as well (Figs. 3 and 4). Therefore, channels are devoid of all major components of the nuclear envelope. This provides a clear entryway into daughter nuclei through which acentrics pass. Aurora B kinase, a well-established inhibitor of nuclear envelope formation, localizes to the tether, where its activity is integral to the formation of these channels (Karg et al., 2015; Warecki and Sullivan, 2018). Failure to form channels results in daughter nuclei completely surrounded by a nuclear envelope and the inability of acentrics to enter nuclei, forming micronuclei (Karg et al., 2015). Taken together, these results indicate that the highly localized inhibition of all components of nuclear envelope reassembly at the site of the channel is required for a neuroblast dividing with late-segregating acentrics to maintain euploidy.

Acentric incorporation involves localized extension and retraction of the nuclear lamina

These results and previous studies (Afonso et al., 2014; Karg et al., 2015; Warecki and Sullivan, 2018) have led to the idea that nuclear envelope reassembly is antagonistic to acentric entry into daughter nuclei. The data presented here demonstrate that while the physical barrier of the nuclear envelope must be bypassed through local inhibition of nuclear envelope assembly, the reassembling nuclear envelope is actively involved in incorporating acentrics into daughter nuclei as well.

We observed lamin extend outward from nuclear envelope channels and toward the poleward-segregating acentrics (Fig. 2). Lamin extensions then retracted back toward nuclei as acentrics passed through channels. This coordinated movement suggests a mechanistic link between the lamin extensions and the acentric passage. While poleward movement occurs through the action of microtubules that bundle around the acentrics (Karg et al., 2017), the forces that drive acentrics through channels remain unknown.

During the time that acentrics pass through channels, we observed a decrease in acentric velocity (Fig. 1). Acentrics initially moved off the metaphase plate at a measured velocity of 10 nm/s, comparable to previously reported segregation rates of undamaged chromosomes in *Drosophila* S2 cells of 9.8 nm/s (de Lartigue et al., 2011). As acentrics passed through channels, their velocities slowed, indicating different and/or additional forces imposed on the acentrics as they entered nuclei. It is tempting to speculate that retracting lamin extensions "take over" from microtubules to drive acentrics into nuclei. However, the mild correlation we measured between lamin retraction and acentric movement suggests that factors in addition to lamin extension and retraction drive acentrics through nuclear envelope channels.

Acentric entry into daughter nuclei results in global changes to nuclear morphology

As the acentric entered the telophase nucleus, we often observed global distortions in the organization of the nuclear envelope. While the elongated shape of nuclei was expected due to lamin extensions emanating from the channels, we were surprised by the presence of distortions and blebs at regions distant from the channel and acentric entry. As a result of these global

distortions, the nuclei exhibited an overall wrinkled appearance. We do not believe that the lamin blebs we observe are nuclear herniations caused by malfunctioning nuclear pore complexes sealed behind a nuclear membrane (Webster et al., 2016). That is, at sites other than the channel, nuclear pore complex assembly appeared normal: GFP-Nup107 clearly localized along the rim of the nucleus, and GFP-NLS accumulated in the daughter nuclei. An explanation for the global distortions in the nuclear envelope upon acentric entry is that restructuring the entire nuclear envelope is required to provide sufficient membrane, lamin, and other components for the channel extensions.

Misshapen nuclei have long been observed in diseased and cancerous cells, including both primary tumors and cultured cell lines (Zink et al., 2004; Goldman et al., 2004; Helfand et al., 2012). Intriguingly, some of the cell lines in which nuclear blebbing has been observed often divide with lagging chromosomes (Wang and Kung, 2012; Cosenza et al., 2017). Abnormal nuclear blebs in these cells were only detected following cell division (Helfand et al., 2012). It would be interesting to see if these cancer cells undergo similar nuclear envelope reassembly modifications to facilitate the incorporation and repair of lagging and broken chromosomes, resulting in blebs.

Acentrics are encompassed by a membrane distinct from the nuclear envelope

In contrast to the composition of the nuclear envelope components at the channel sites, in which all three major components were excluded from the sites of acentric entry to form nuclear envelope channels, we observed nuclear membrane localize to late-segregating acentrics despite the absence of lamin and nuclear pore complexes (Fig. 3). We demonstrated the presence of nuclear membrane on acentrics by using superresolution microscopy to show that the INM protein Otefin is enriched on late-segregating acentrics (Fig. 3) and by using the luminal ER marker PDI-GFP (Fig. 4). We also found that acentrics were enriched with BAF, a protein that can recruit INM proteins and nuclear membrane to the sites of nuclear envelope ruptures in interphase (Halfmann et al., 2019). The difference in the ability of core and noncore components of the nuclear envelope to localize to lagging chromosomes was previously observed in cancer cells in which lagging whole chromosomes subsequently formed micronuclei (Liu et al., 2018). A key difference between this finding and ours is that the membrane-coated acentrics in our study remain capable of reentering daughter nuclei, whereas the lagging whole chromosomes do not.

Membrane fusion drives the final stage of acentric incorporation into daughter nuclei

At the time when acentrics enter daughter nuclei, there appears to be fusion between the membrane on the acentrics and the membrane on the daughter nuclei (Fig. 4). Membrane fusion between the acentric and the daughter nucleus could explain how membrane-encapsulated acentrics remain capable of entering daughter nuclei. We hypothesized that membrane fusion between membrane on acentrics and membrane on daughter nuclei would be required for acentric integration into daughter nuclei.

Warecki et al.
ESCRT-III drives chromosome fragments into nuclei

Journal of Cell Biology   16 of 22
https://doi.org/10.1083/jcb.201905091

In accord with this hypothesis, we observed decreased acentric entry into daughter nuclei when cells were depleted of the conserved membrane fusion proteins Comt/NSF and Shrub/CHMP4B (Fig. 5). In the canonical model of membrane fusion, the assembly of SNAREs on opposing membranes into a trans-SNARE complex mediates fusion of the membranes. NSF uses ATP hydrolysis to disassemble the trans-SNARE complex, freeing SNAREs for additional rounds of membrane fusion (Ryu et al., 2016). SNARE and NSF membrane fusion activity are essential for proper nuclear envelope reassembly: mutants result in membrane targeting to, but not sealing around, daughter nuclei (Baur et al., 2007). We believe the failure of acentric entry into daughter nuclei in Comt-depleted neuroblasts is due to an inability of these cells to undergo repeated rounds of SNARE-mediated membrane fusion necessary to fuse the membrane on acentrics to the membrane on nuclei.

Like Comt/NSF, Shrub/CHMP4B has conserved membrane fusion functions. CHMP4B is a major component of the ESCRT-III complex, which mediates membrane fusion in many processes, including cytokinesis (Carlton and Martin-Serrano, 2007; Morita et al., 2007), viral budding (Arii et al., 2018; Johnson et al., 2018), and plasma membrane repair (Jimenez et al., 2014). Recent work has shown that ESCRT-III also mediates membrane sealing during nuclear envelope reassembly (Vietri et al., 2015; Olmos et al., 2015) and nuclear envelope repair (Denais et al., 2016; Raab et al., 2016). Previous studies have shown that ESCRT-III localizes to lagging chromosomes that form micronuclei (Liu et al., 2018) and to micronuclei in interphase (Sagona et al., 2014; Willan et al., 2019). In these cells, ESCRT-III seals the nuclear membrane around the lagging chromosome and prevents proper recruitment of nuclear pore complexes, which can subsequently lead to increased chromothripsis (Liu et al., 2018). In addition, ESCRT-III activity on micronuclei in interphase may also lead to micronuclei degradation through autophagy (Sagona et al., 2014).

In contrast to these reports, in which ESCRT-III activity results in the damage to or loss of key genetic information, we believe ESCRT-III activity on late-segregating acentrics in *Drosophila* neuroblasts promotes maintenance of euploidy. We observed a failure of acentrics to enter into daughter nuclei in Shrub/CHMP4B-depleted neuroblasts. We also observed failed acentric entry when neuroblasts were depleted of a second ESCRT-III component, CHMP2B. Additionally, we found that Shrub localized to acentrics during acentric reintegration into daughter nuclei but not during acentric initial poleward movement (Fig. 5), suggesting that the main activity of ESCRT-III on acentrics is during reintegration. We hypothesize that the failure of acentrics to enter daughter nuclei when ESCRT-III components are depleted is likely due to the same inability to fuse membrane on acentrics to membrane on daughter nuclei as we believe occurs in Comt-depleted cells. This could mechanistically explain the previously reported increase in the frequency of cells with micronuclei observed when ESCRT-III components are depleted (Willan et al., 2019).

Finally, we found that efficient acentric reintegration was dependent on the ER protein Rtnl2/RTN2 (Fig. 5). Rtnl2 is a member of the reticulon family, a group of proteins that play crucial roles in restructuring the ER throughout the cell cycle, including during mitosis (Voeltz et al., 2006). Reticulon proteins stabilize areas of high membrane curvature (Voeltz et al., 2006), and altering the levels of different reticulons in the cell can affect the dynamics of nuclear envelope reassembly (Anderson and Hetzer, 2008). It is possible that Rtnl2 is required to form or stabilize curved nuclear membranes that may manifest as acentrics enter daughter nuclei. Failure to form these curved membranes in Rtnl2 knockdowns may prevent fusion between acentric-associated and daughter nuclei–associated membrane, ultimately resulting in micronucleus formation.

Nuclear envelope channels may be recognized as ruptured nuclear envelopes

We believe membrane fusion–mediated acentric reintegration into daughter nuclei is most analogous to the repair of nuclear envelope ruptures. Mechanical stress can cause nuclear envelope rupture in interphase cells (Denais et al., 2016; Raab et al., 2016). Ruptures create lamin- and nuclear pore complex–free membrane blebs through which chromatin protrudes, followed by membrane breakage (Denais et al., 2016). BAF is enriched at the site of the rupture (Halfmann et al., 2019). BAF in turn recruits LEM-domain proteins and membrane (Halfmann et al., 2019). Finally, ESCRT-III activity restores nuclear envelope integrity (Raab et al., 2016; Denais et al., 2016). ESCRT-III can similarly repair ruptured membranes that occur on interphase micronuclei (Willan et al., 2019), indicating that repair is not limited to primary nuclei.

We observe strikingly similar events in cells with acentrics entering daughter nuclei through nuclear envelope channels. There are lamin- and nuclear pore complex–free gaps in the nuclear envelope at the site of channels with membrane-coated chromatin "protruding" (acentrics). We observed enriched BAF on late-segregating acentrics as well as enriched Otefin (Fig. 4). Canonical membrane fusion proteins and ESCRT-III are required to bring the acentric through the channel and into the nucleus, after which lamin and nuclear pore complexes are recruited over the channel opening, thus "repairing" the channel. Because the channel is not a feature of normal nuclear envelope reassembly (Karg et al., 2015), it is possible that the cell recognizes channels as ruptured nuclei, even though channels and ruptures result from separate mechanisms. If this were the case, it would be interesting to understand how the cell establishes that the segregating acentric belongs with the daughter nucleus. It seems likely this is due to the tether connecting the acentric to the nucleus (Royou et al., 2010). BAF, which we observed strongly accumulating on acentrics (Fig. 4), cross-bridges DNA in anaphase/telophase to ensure that a nuclear envelope surrounds chromosomes in normal divisions (Samwer et al., 2017). We also observed BAF on the tether where it perhaps performs a similar role.

The work presented here focuses on the final steps in which late-segregating chromatids enter daughter nuclei. In summary, our results support a model in which fusion of the reassembling nuclear membrane drives entry of chromosome fragments into daughter nuclei (Fig. 7). To our knowledge, this represents a novel mechanism by which cells dividing with lagging chromosomes are able to maintain their genome integrity.
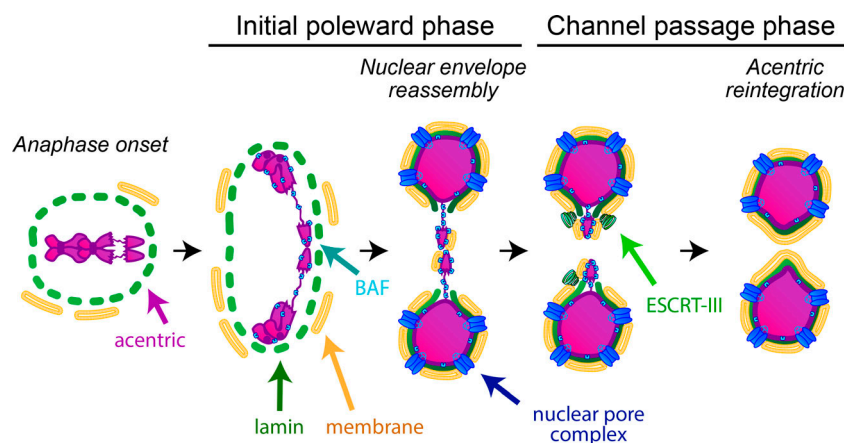
Figure 7. **Model for membrane fusion-mediated acentric reintegration into daughter nuclei.** Acentrics (magenta arrow) lag behind on the metaphase plate while the undamaged sister chromatids segregate. Acentrics remain connected to daughter nuclei by a previously described DNA tether (Royou et al., 2010). In late anaphase, acentrics begin segregating poleward via the action of microtubules (not depicted). In telophase, all three major components of the nuclear envelope (dark green arrow, lamin; blue arrow, nuclear pore complexes; yellow arrow, membrane) assemble on daughter nuclei, but only membrane assembles on acentrics. Nuclear envelope channels form in the lamin, nuclear pore complex, and membrane on daughter nuclei to provide a passageway through which acentrics can enter nuclei. BAF (cyan) localizes to channels, tethers, and acentrics. Membrane fusion proteins such as NSF and ESCRT-III (light green arrow) localize to acentrics and daughter nuclei at the sites where acentrics first contact nuclei and mediate fusion between the membrane that is on acentrics and the membrane that is on daughter nuclei. These membrane fusion events guide acentrics through channels and into nuclei, allowing the dividing cell to maintain euploidy.

Materials and methods

Drosophila stocks

All *Drosophila* stocks were raised on brown food (Sullivan et al., 2000). Crosses were performed at 25°C with the exception of crosses involving Shrub-GFP (Fig. 6), which were performed at 18°C. Chromosome behavior was monitored using H2Av-RFP (stock #23561; Bloomington Drosophila Stock Center [BDSC]). elav-Gal4 (Lin and Goodman, 1994) was used to drive expression of transgenes under control of an upstream activating sequence (UAS). We used the following lines to monitor nuclear envelope components: UAS-Lamin-GFP (#7376; BDSC), GFP-Nup107 (#35514; BDSC), and PDI-GFP (#6839; BDSC). *y1v1* flies (#1509) were used as a control for the RNAi screen (Table 1). The following RNAi lines were obtained from BDSC: UAS-Rtnl2-shRNA (#58208), UAS-Shrub-shRNA (#38305), UAS-Comt-shRNA (#31666, #31470), UAS-CHMP2B-shRNA (#28531), UAS-Snap24-shRNA (#28719), UAS-Membrin-shRNA (#50515), UAS-Snap-shRNA (#29587), UAS-Spastin-shRNA (#53331), UAS-Atlastin-shRNA (#36736), UAS-Usnp-shRNA (#25862), UAS-Syb-shRNA (#38234), and UAS-Snap25-shRNA (#34377). We rebalanced RNAi stocks originally segregating Cyo to now segregate Cyo-GFP to allow for selection of the RNAi transgene at the larval stage. In addition, we used the following mutant flies: *comt6* (#26708; BDSC) and *Rtnl1* (#12425; BDSC). Flies containing UAS-Shrub-GFP and GFP-BAF transgenes were generously provided by Dr. Fen-Biao Gao (University of Massachusetts Medical School, Worcester, MA) and Dr. Pamela Geyer (University of Iowa, Iowa City, IA), respectively.

Fixed neuroblast cytology

Fixed samples were prepared by heat shocking female third-instar larvae bearing I-CreI for 1 h at 37°C. After 1- h recovery, brains were dissected in 0.7% NaCl and fixed in 3.7% formal-dehyde for 30 min. Brains were washed in 45% acetic acid in PBS and then squashed between siliconized coverslips and glass slides in 60% acetic acid. Brains were gently squashed and then frozen in liquid nitrogen for at least 10 min. After washes in 20% ethanol (10 min at –20°C), PBS with Triton X-100 (PBST; 10 min), and PBS (2 × 5 min), slides were blocked in 5% dried milk in PBST for 1 h at room temperature. Samples were incubated with goat anti-Otefin (Barton et al., 2014), provided by Dr. Pamela Geyer, at a 1:500 dilution overnight at 4°C. Samples were washed three times in PBST and stained with donkey anti-goat Alexa Fluor 488 (Invitrogen #A-11055) at a 1:300 dilution for 1 h at room temperature. Samples were again washed three times in PBST and counterstained with DAPI in Vectashield (Vector H-1200).

Live neuroblast cytology

For experiments involving live imaging of acentrics, crawling female third-instar larvae were heat shocked for 1 h at 37°C. After larvae recovered for 1–6 h at room temperature, brains were dissected in PBS and squashed in 17 µl of PBS between a slide and coverslip. Excess PBS was wicked away (Buffin et al., 2005). Coverslips were outlined with halocarbon oil, and imaging was performed immediately. We filmed neuroblasts along the periphery of the squashed brain. Slides were imaged for up to 1 h.

Microscopy and image acquisition

Wide-field microscopy

Time-lapse imaging for the RNAi screen was performed using a Leica DM16000B wide-field inverted microscope equipped with a Hamamatsu electron-multiplying charge coupled device camera (ORCA 9100-02) with a binning of 1 and a 100× Plan-Apochromat objective with NA 1.4, as well as with a spinning-disk confocal microscope (described below). Successive time points were filmed at 20 s on the wide-field microscope. RFP (585 nm) and GFP (508 nm) fluorophores were imaged. Samples were imaged in PBS. Microscopy was performed at room temperature (20–22°C). Wide-field images were acquired with Leica

Application Suite Advanced Fluorescence software and 3D deconvolved using AutoQuant X2.2.0 software.

Spinning-disk microscopy

Time-lapse imaging for the RNAi screen was performed using an inverted Eclipse TE2000-E spinning-disk (CSLI-X1; Nikon) confocal microscope equipped with a Hamamatsu electron-multiplying charge coupled device camera (ImageEM X2) with a 100× 1.4-NA oil-immersion objective and a wide-field microscope (described above). Samples were imaged in PBS. 488- and 561-nm lasers were used to excite GFP and RFP fluorophores. Spinning-disk microscopy was performed at room temperature (20–22°C). Successive time points were filmed at 10–18 s on the spinning-disk microscope. Spinning-disk images were acquired with MicroManager 1.4 software.

All imaging experiments involving distance and fluorescence quantification (Figs. 1, A–D and F–H; 2, A–D; 3, A and B; 4, A, A', D, and D'; 5 A'–D'; 6; and S4) were performed exclusively using the Nikon Eclipse TE2000-E spinning-disk microscope. Successive time points for experiments presented in Figs. 1, A–D; 2, A–D; 3, A and B; 4; and 6 were filmed at 18 s. Successive time points for experiments presented in Fig. 5 A'–D', were filmed at 10 s.

The distances of acentrics to daughter nuclei were calculated either as the distance of the farthest point on the acentric to the nearest point on the daughter nucleus (Figs. 1 H, 2 D, and 5 A'–D') or as the distance of the nearest point on the acentric to the nearest point on the daughter nucleus (Figs. 1 D, 2 C, and S2 A). Distances were calculated at the time points indicated in the sections describing each figure. The lengths of lamin extensions were measured from the nearest point on the nucleus to the farthest point of the extension (Fig. 2, B–D) at the time points indicated in descriptions of each panel. All distances were measured in 3D space (z-spacing = 360 nm) from Z-stacks taken during spinning-disk microscopy and were performed in Fiji (Schindelin et al., 2012).

The distances of acentrics from daughter nuclei in our RNAi screen (Fig. S2 A) were measured as described above. Distances were measured at the point when acentrics began their poleward movement. The time of acentric segregation (Fig. S2 B) was determined by measuring the time between anaphase onset and when acentrics first began their poleward movement. Distance measurements were made only on videos acquired using spinning-disk confocal microscopy, while time measurements were made on videos filmed both with the wide-field and spinning-disk microscopes.

Quantitative measurements of nuclear envelope components on acentrics (Fig. 3, A' and B'; and Fig. 4, A' and D') were made in Fiji. We used sum projections for all fluorescence quantification measurements. We created a region of interest around the acentric or nucleus at each time point and measured the background-subtracted fluorescence intensity of the GFP signal for the drawn region (Fig. S1). Intensities were divided by the areas of the regions of interest. Each acentric was paired with the nucleus to which it was segregating. All values in an acentric/nucleus pair were then normalized to the highest value in the acentric/nucleus pair.

Quantitative measurements of GFP-NLS on nuclei (Fig. 1, A–D; and Fig. S4) were made in Fiji using sum projections. Nucleus/cytoplasm ratios were determined by dividing the background-subtracted average pixel intensities of the nuclei by the background-subtracted average pixel intensities of a region in the cytoplasm.

Airyscan microscopy

All superresolution images were acquired with an AxioObserver.Z1 Zeiss 880 confocal microscope equipped with an Airyscan detector and a 63× 1.4-NA Plan-Apochromat objective. Samples were imaged in Vectashield mounting medium containing DAPI (Vector H-1200). Data were collected using a dual bandpass filter (420–480 nm for DAPI and 495–550 nm for Alexa Fluor 488). Imaging was performed at room temperature. 405- and 488-nm lasers were used to image DAPI and Alexa Fluor 488 fluorophores. Images were collected using the normal Airyscan mode with Zen Black software (Zeiss) and deconvolved using Zen Blue (Zeiss).

Lattice light-sheet microscopy

We performed lattice light-sheet microscopy using the custom-built lattice light-sheet microscope at the Advanced Imaging Center of the Howard Hughes Medical Institute Janelia research campus (Ashburn, VA). Larvae were prepared as described above. After dissection, whole brains were mounted unsquashed in a drop of ~2% agarose. Before imaging, mounted brains were placed on ice for 30 s and then imaged in a slide bath containing PBS. Brains were excited by a Special Optics 0.65-NA 3.74-mm working water dipping objective and detected with a Nikon chrome-free infinity-corrected Apo long working distance 25X water dipping 1.1-NA objective, 63× magnification. Neuroblast divisions were filmed with a Hamamatsu Orca Flash 4.0 v2 scientific complementary metal oxide semiconductor camera. 560- and 488-nm lasers were used to image RFP and GFP fluorophores. Imaging was performed at room temperature. Time-lapse videos were deskewed and deconvolved using Janelia software (Chen et al., 2014) before analysis.

The sphericities of daughter nuclei (Fig. 2 F) were measured in Imaris v9.2 (Bitplane) by generating contour surfaces of the nuclear envelopes at the time of completed lamin reassembly (Fig. 2 E, right panels). We used Imaris software to draw regions of interest that aligned to the peripheral fluorescence intensity of Lamin-GFP in successive cross sections throughout each Z-plane of the nucleus. These regions were then used to construct the surface using the contour surface tool in Imaris software. Sphericity values were calculated from the constructed surfaces.

Statistical analyses

All statistical tests were performed in R (R Core Team). We used the following tests: a two-sided Wilcoxon signed-rank test (Fig. 1 H), a paired two-sided t test (Fig. 2 B), independent two-sided t tests (Fig. S2 B), two-sided Mann–Whitney–Wilcoxon tests (Figs. 1 C, 2 F, and S2 A), χ^2 tests (Fig. 5), and a Schierer–Ray–Hare test (Fig. S4 C'). For the parametric tests performed, normality was first determined visually and then by running Shapiro–Wilk normality tests (Fig. 2 B: longest extension, P = 0.9;

reassembly completed, P = 0.5; Fig. S2 B: control, P = 0.4; Comt RNAi, P = 0.5; Rtnl2 RNAi, P = 0.06; and Shrub RNAi, P = 0.9). For all other cases, in which data were not normally distributed, nonparametric tests were used. Additionally, we calculated the Pearson's correlations for data presented in Fig. 2, C and D, in R.

Figure and video preparation

Figures were assembled in Adobe Illustrator. Imaging data were processed in Fiji. In all cases, unless otherwise noted, maximum projections are shown. Selected images were adjusted for brightness and contrast to improve clarity when appropriate. For videos only, a rigid body registration (Fiji plugin StackReg) was used to correct for cell movement, if necessary, to reduce file size. Images for experiments involving lattice light-sheet microscopy were processed and analyzed using Imaris. Graphs were created in R using the ggplot2 package (Wickham, 2016).

Online supplemental material

Fig. S1 shows a diagram for how fluorescence intensities were calculated on acentrics and daughter nuclei for experiments in Figs. 3 A′ and B′, and 4 A′ and D′. Fig. S2 shows the distance of acentrics from nuclei at the time of acentric segregation and the time from anaphase onset to acentric segregation for control, Comt-, Rtnl2-, and Shrub-depleted neuroblasts, and corresponds with Fig. 5, A–D. Fig. S3 shows a diagram illustrating how the distance between acentrics and daughter nuclei in divisions in which acentrics that reenter daughter nuclei approaches 0 and that of divisions in which acentrics that form daughter nuclei will be >0, corresponding with Fig. 5, A′–D′. Fig. S4 shows that Comt-depleted neuroblasts have acentrics that form micronuclei despite GFP-NLS recruitment to daughter nuclei. Video 1 is from Fig. 1 F. Video 2 is from Fig. 2 A. Video 3 is from Fig. 3 A. Video 4 is from Fig. 3 B. Video 5 is from Fig. 4 A. Video 6 is from Fig. 5 A. Video 7 is from Fig. 5 B. Video 8 is from Fig. 5 C. Video 9 is from Fig. 5 D. Video 10 is from Fig. 6 A.

Acknowledgments

References

Afonso, O., I. Matos, A.J. Pereira, P. Aguiar, M.A. Lampson, and H. Maiato. 2014. Feedback control of chromosome separation by a midzone Aurora B gradient. *Science.* 345:332–336. https://doi.org/10.1126/science.1251121

Anderson, D.J., and M.W. Hetzer. 2008. Reshaping of the endoplasmic reticulum limits the rate for nuclear envelope formation. *J. Cell Biol.* 182: 911–924. https://doi.org/10.1083/jcb.200805140

Anderson, D.J., J.D. Vargas, J.P. Hsiao, and M.W. Hetzer. 2009. Recruitment of functionally distinct membrane proteins to chromatin mediates nuclear envelope formation in vivo. *J. Cell Biol.* 186(2):183–191. https://doi.org/10.1083/jcb.200901106

Arii, J., M. Watanabe, F. Maeda, N. Tokai-Nishizumi, T. Chihara, M. Miura, Y. Maruzuru, N. Koyanagi, A. Kato, and Y. Kawaguchi. 2018. ESCRT-III mediates budding across the inner nuclear membrane and regulates its integrity. *Nat. Commun.* 9:3379. https://doi.org/10.1038/s41467-018-05889-9

Ashery-Padan, R., N. Ulitzur, A. Arbel, M. Goldberg, A.M. Weiss, N. Maus, P.A. Fisher, and Y. Gruenbaum. 1997. Localization and posttranslational modifications of otefin, a protein required for vesicle attachment to chromatin, during Drosophila melanogaster development. *Mol. Cell. Biol.* 17:4114–4123. https://doi.org/10.1128/MCB.17.7.4114

Barton, L.J., B.S. Pinto, L.L. Wallrath, and P.K. Geyer. 2013. The Drosophila nuclear lamina protein otefin is required for germline stem cell survival. *Dev. Cell.* 25:645–654. https://doi.org/10.1016/j.devcel.2013.05.023

Barton, L.J., S.R. Wilmington, M.J. Martin, H.M. Skopec, K.E. Lovander, B.S. Pinto, and P.K. Geyer. 2014. Unique and shared functions of nuclear lamina LEM domain proteins in *Drosophila*. *Genetics.* 197:653–665. https://doi.org/10.1534/genetics.114.162941

Baur, T., K. Ramadan, A. Schlundt, J. Kartenbeck, and H.H. Meyer. 2007. NSF- and SNARE-mediated membrane fusion is required for nuclear envelope formation and completion of nuclear pore complex assembly in Xenopus laevis egg extracts. *J. Cell Sci.* 120:2895–2903. https://doi.org/10.1242/jcs.010181

Bergman, Z.J., J.D. Mclaurin, A.S. Eritano, B.M. Johnson, A.Q. Sims, and B. Riggs. 2015. Spatial reorganization of the endoplasmic reticulum during mitosis relies on mitotic kinase cyclin A in the early *Drosophila* embryo. *PLoS One.* 10:e0117859. https://doi.org/10.1371/journal.pone.0117859

Bobinnec, Y., C. Marcaillou, X. Morin, and A. Debec. 2003. Dynamics of the endoplasmic reticulum during early development of Drosophila melanogaster. *Cell Motil. Cytoskeleton.* 54:217–225. https://doi.org/10.1002/cm.10094

Bonassi, S., R. El-Zein, C. Bolognesi, and M. Fenech. 2011. Micronuclei frequency in peripheral blood lymphocytes and cancer risk: evidence from human studies. *Mutagenesis.* 26:93–100. https://doi.org/10.1093/mutage/geq075

Bretscher, H.S., and D.T. Fox. 2016. Proliferation of Double-Strand Break-Resistant Polyploid Cells Requires Drosophila FANCD2. *Dev. Cell.* 37: 444–457. https://doi.org/10.1016/j.devcel.2016.05.004

Buffin, E., C. Lefebvre, J. Huang, M.E. Gagou, and R.E. Karess. 2005. Recruitment of Mad2 to the kinetochore requires the Rod/Zw10 complex. *Curr. Biol.* 15:856–861. https://doi.org/10.1016/j.cub.2005.03.052

Carlson, J.G. 1938. Mitotic Behavior of Induced Chromosomal Fragments Lacking Spindle Attachments in the Neuroblasts of the Grasshopper. *Proc. Natl. Acad. Sci. USA.* 24:500–507. https://doi.org/10.1073/pnas.24.11.500

Carlton, J.G., and J. Martin-Serrano. 2007. Parallels between cytokinesis and retroviral budding: a role for the ESCRT machinery. *Science.* 316: 1908–1912. https://doi.org/10.1126/science.1143422

Champion, L., S. Pawar, N. Luithle, R. Ungricht, and U. Kutay. 2019. Dissociation of membrane-chromatin contacts is required for proper

chromosome segregation in mitosis. *Mol. Biol. Cell.* 30:427–440. https://doi.org/10.1091/mbc.E18-10-0609

Chaudhary, N., and J.C. Courvalin. 1993. Stepwise reassembly of the nuclear envelope at the end of mitosis. *J. Cell Biol.* 122:295–306. https://doi.org/10.1083/jcb.122.2.295

Chen, B.C., W.R. Legant, K. Wang, L. Shao, D.E. Milkie, M.W. Davidson, C. Janetopoulos, X.S. Wu, J.A. Hammer III, Z. Liu, et al. 2014. Lattice light-sheet microscopy: imaging molecules to embryos at high spatiotemporal resolution. *Science.* 346:1257998. https://doi.org/10.1126/science.1257998

Cosenza, M.R., A. Cazzola, A. Rossberg, N.L. Schieber, G. Konotop, E. Bausch, A. Slynko, T. Holland-Letz, M.S. Raab, T. Dubash, et al. 2017. Asymmetric Centriole Numbers at Spindle Poles Cause Chromosome Missegregation in Cancer. *Cell Reports.* 20:1906–1920. https://doi.org/10.1016/j.celrep.2017.08.005

Crasta, K., N.J. Ganem, R. Dagher, A.B. Lantermann, E.V. Ivanova, Y. Pan, L. Nezi, A. Protopopov, D. Chowdhury, and D. Pellman. 2012. DNA breaks and chromosome pulverization from errors in mitosis. *Nature.* 482: 53–58. https://doi.org/10.1038/nature10802

de Castro, I.J., R.S. Gil, L. Ligammari, M.L. Di Giacinto, and P. Vagnarelli. 2017. CDK1 and PLK1 coordinate the disassembly and reassembly of the nuclear envelope in vertebrate mitosis. *Oncotarget.* 9:7763–7773. https://doi.org/10.18632/oncotarget.23666

de Lartigue, J., I. Brust-Mascher, and J.M. Scholey. 2011. Anaphase B spindle dynamics in Drosophila S2 cells: Comparison with embryo spindles. *Cell Div.* 6:8. https://doi.org/10.1186/1747-1028-6-8

Denais, C.M., R.M. Gilbert, P. Isermann, A.L. McGregor, M. te Lindert, B. Weigelin, P.M. Davidson, P. Friedl, K. Wolf, and J. Lammerding. 2016. Nuclear envelope rupture and repair during cancer cell migration. *Science.* 352:353–358. https://doi.org/10.1126/science.aad7297

Ellenberg, J., E.D. Siggia, J.E. Moreira, C.L. Smith, J.F. Presley, H.J. Worman, and J. Lippincott-Schwartz. 1997. Nuclear membrane dynamics and reassembly in living cells: targeting of an inner nuclear membrane protein in interphase and mitosis. *J. Cell Biol.* 138:1193–1206. https://doi.org/10.1083/jcb.138.6.1193

Fenech, M., M. Kirsch-Volders, A.T. Natarajan, J. Surralles, J.W. Crott, J. Parry, H. Norppa, D.A. Eastmond, J.D. Tucker, and P. Thomas. 2011. Molecular mechanisms of micronucleus, nucleoplasmic bridge and nuclear bud formation in mammalian and human cells. *Mutagenesis.* 26: 125–132. https://doi.org/10.1093/mutage/geq052

Goldman, R.D., D.K. Shumaker, M.R. Erdos, M. Eriksson, A.E. Goldman, L.B. Gordon, Y. Gruenbaum, S. Khuon, M. Mendez, R. Varga, and F.S. Collins. 2004. Accumulation of mutant lamin A causes progressive changes in nuclear architecture in Hutchinson-Gilford progeria syndrome. *Proc. Natl. Acad. Sci. USA.* 101:8963–8968. https://doi.org/10.1073/pnas.0402943101

Green, R.A., and K.B. Kaplan. 2003. Chromosome instability in colorectal tumor cells is associated with defects in microtubule plus-end attachments caused by a dominant mutation in APC. *J. Cell Biol.* 163:949–961. https://doi.org/10.1083/jcb.200307070

Halfmann, C.T., R.M. Sears, A. Katiyar, B.W. Busselman, L.K. Aman, Q. Zhang, C.S. O'Bryan, T.E. Angelini, T.P. Lele, and K.J. Roux. 2019. Repair of nuclear ruptures requires barrier-to-autointegration factor. *J. Cell Biol.* 218:2136–2149. https://doi.org/10.1083/jcb.201901116

Haraguchi, T., T. Koujin, M. Segura-Totten, K.K. Lee, Y. Matsuoka, Y. Yoneda, K.L. Wilson, and Y. Hiraoka. 2001. BAF is required for emerin assembly into the reforming nuclear envelope. *J. Cell Sci.* 114:4575–4585.

Hatch, E.M., A.H. Fischer, T.J. Deerinck, and M.W. Hetzer. 2013. Catastrophic nuclear envelope collapse in cancer cell micronuclei. *Cell.* 154:47–60. https://doi.org/10.1016/j.cell.2013.06.007

Helfand, B.T., Y. Wang, K. Pfleghaar, T. Shimi, P. Taimen, and D.K. Shumaker. 2012. Chromosomal regions associated with prostate cancer risk localize to lamin B-deficient microdomains and exhibit reduced gene transcription. *J. Pathol.* 226:735–745. https://doi.org/10.1002/path.3033

Huang, Y., L. Jiang, Q. Yi, L. Lv, Z. Wang, X. Zhao, L. Zhong, H. Jiang, S. Rasool, Q. Hao, et al. 2012. Lagging chromosomes entrapped in micronuclei are not 'lost' by cells. *Cell Res.* 22:932–935. https://doi.org/10.1038/cr.2012.26

Jimenez, A.J., P. Maiuri, J. Lafaurie-Janvore, S. Divoux, M. Piel, and F. Perez. 2014. ESCRT machinery is required for plasma membrane repair. *Science.* 343:1247136. https://doi.org/10.1126/science.1247136

Johnson, D.S., M. Bleck, and S.M. Simon. 2018. Timing of ESCRT-III protein recruitment and membrane scission during HIV-1 assembly. *eLife.* 7: e36221. https://doi.org/10.7554/eLife.36221

Karg, T., M.W. Elting, H. Vicars, S. Dumont, and W. Sullivan. 2017. The chromokinesin Klp3a and microtubules facilitate acentric chromosome

segregation. *J. Cell Biol.* 216:1597–1608. https://doi.org/10.1083/jcb.201604079

Karg, T., B. Warecki, and W. Sullivan. 2015. Aurora B-mediated localized delays in nuclear envelope formation facilitate inclusion of late-segregating chromosome fragments. *Mol. Biol. Cell.* 26:2227–2241. https://doi.org/10.1091/mbc.E15-01-0026

Katsani, K.R., R.E. Karess, N. Dostatni, and V. Doye. 2008. In vivo dynamics of Drosophila nuclear envelope components. *Mol. Biol. Cell.* 19:3652–3666. https://doi.org/10.1091/mbc.e07-11-1162

Kotadia, S., E. Montembault, W. Sullivan, and A. Royou. 2012. Cell elongation is an adaptive response for clearing long chromatid arms from the cleavage plane. *J. Cell Biol.* 199:745–753. https://doi.org/10.1083/jcb.201208041

Krishnan, K.S., S. Chakravarty, S. Rao, V. Raghuram, and M. Ramaswami. 1996. Alleviation of the temperature-sensitive paralytic phenotype of shibire(ts) mutants in Drosophila by sub-anesthetic concentrations of carbon dioxide. *J. Neurogenet.* 10:221–238. https://doi.org/10.3109/01677069609083464

Liang, H., W.H. Wright, S. Cheng, W. He, and M.W. Berns. 1993. Micromanipulation of chromosomes in PTK2 cells using laser microsurgery (optical scalpel) in combination with laser-induced optical force (optical tweezers). *Exp. Cell Res.* 204:110–120. https://doi.org/10.1006/excr.1993.1015

Lin, D.M., and C.S. Goodman. 1994. Ectopic and increased expression of Fasciclin II alters motoneuron growth cone guidance. *Neuron.* 13: 507–523. https://doi.org/10.1016/0896-6273(94)90022-1

Liu, S., M. Kwon, M. Mannino, N. Yang, F. Renda, A. Khodjakov, and D. Pellman. 2018. Nuclear envelope assembly defects link mitotic errors to chromothripsis. *Nature.* 561:551–555. https://doi.org/10.1038/s41586-018-0534-z

Ly, P., L.S. Teitz, D.H. Kim, O. Shoshani, H. Skaletsky, D. Fachinetti, D.C. Page, and D.W. Cleveland. 2017. Selective Y centromere inactivation triggers chromosome shattering in micronuclei and repair by non-homologous end joining. *Nat. Cell Biol.* 19:68–75. https://doi.org/10.1038/ncb3450

Maass, K.K., F. Rosing, P. Ronchi, K.V. Willmund, F. Devens, M. Hergt, H. Herrmann, P. Lichter, and A. Ernst. 2018. Altered nuclear envelope structure and proteasome function of micronuclei. *Exp. Cell Res.* 371: 353–363. https://doi.org/10.1016/j.yexcr.2018.08.029

Mikhailov, A., R.W. Cole, and C.L. Rieder. 2002. DNA damage during mitosis in human cells delays the metaphase/anaphase transition via the spindle-assembly checkpoint. *Curr. Biol.* 12:1797–1806. https://doi.org/10.1016/S0960-9822(02)01226-5

Montembault, E., M.C. Claverie, L. Bouit, C. Landmann, J. Jenkins, A. Tsankova, C. Cabernard, and A. Royou. 2017. Myosin efflux promotes cell elongation to coordinate chromosome segregation with cell cleavage. *Nat. Commun.* 8:326. https://doi.org/10.1038/s41467-017-00337-6

Montenegro, G., A.P. Rebelo, J. Connell, R. Allison, C. Babalini, M. D'Aloia, P. Montieri, R. Schüle, H. Ishiura, J. Price, et al. 2012. Mutations in the ER-shaping protein reticulon 2 cause the axon-degenerative disorder hereditary spastic paraplegia type 12. *J. Clin. Invest.* 122:538–544. https://doi.org/10.1172/JCI60560

Morita, E., V. Sandrin, H.Y. Chung, S.G. Morham, S.P. Gygi, C.K. Rodesch, and W.I. Sundquist. 2007. Human ESCRT and ALIX proteins interact with proteins of the midbody and function in cytokinesis. *EMBO J.* 26: 4215–4227. https://doi.org/10.1038/sj.emboj.7601850

Olmos, Y., L. Hodgson, J. Mantell, P. Verkade, and J.G. Carlton. 2015. ESCRT-III controls nuclear envelope reformation. *Nature.* 522:236–239 https://doi.org. https://doi.org/10.1038/nature14503

Ordway, R.W., L. Pallanck, and B. Ganetzky. 1994. Neurally expressed Drosophila genes encoding homologs of the NSF and SNAP secretory proteins. *Proc. Natl. Acad. Sci. USA.* 91:5715–5719. https://doi.org/10.1073/pnas.91.12.5715

Pidoux, A.L., S. Uzawa, P.E. Perry, W.Z. Cande, and R.C. Allshire. 2000. Live analysis of lagging chromosomes during anaphase and their effect on spindle elongation rate in fission yeast. *J. Cell Sci.* 113:4177–4191.

Raab, M., M. Gentili, H. de Belly, H.R. Thiam, P. Vargas, A.J. Jimenez, F. Lautenschlaeger, R. Voituriez, A.M. Lennon-Duménil, N. Manel, and M. Piel. 2016. ESCRT III repairs nuclear envelope ruptures during cell migration to limit DNA damage and cell death. *Science.* 352:359–362. https://doi.org/10.1126/science.aad7611

Riemer, D., N. Stuurman, M. Berrios, C. Hunter, P.A. Fisher, and K. Weber. 1995. Expression of Drosophila lamin C is developmentally regulated: analogies with vertebrate A-type lamins. *J. Cell Sci.* 108:3189–3198.

Rong, Y.S., S.W. Titen, H.B. Xie, M.M. Golic, M. Bastiani, P. Bandyopadhyay, B.M. Olivera, M. Brodsky, G.M. Rubin, and K.G. Golic. 2002. Targeted

mutagenesis by homologous recombination in D. melanogaster. *Genes Dev.* 16:1568–1581. https://doi.org/10.1101/gad.986602

Royou, A., M.E. Gagou, R. Karess, and W. Sullivan. 2010. BubR1- and Polo-coated DNA tethers facilitate poleward segregation of acentric chromatids. *Cell.* 140:235–245. https://doi.org/10.1016/j.cell.2009.12.043

Ryu, J.K., R. Jahn, and T.Y. Yoon. 2016. Review: Progresses in understanding N-ethylmaleimide sensitive factor (NSF) mediated disassembly of SNARE complexes. *Biopolymers.* 105:518–531. https://doi.org/10.1002/bip.22854

Sabatinos, S.A., N.S. Ranatunga, J.P. Yuan, M.D. Green, and S.L. Forsburg. 2015. Replication stress in early S phase generates apparent micronuclei and chromosome rearrangement in fission yeast. *Mol. Biol. Cell.* 26:3439–3450. https://doi.org/10.1091/mbc.E15-05-0318

Sacristan, C., and G.J. Kops. 2015. Joined at the hip: kinetochores, microtubules, and spindle assembly checkpoint signaling. *Trends Cell Biol.* 25:21–28. https://doi.org/10.1016/j.tcb.2014.08.006

Sagona, A.P., I.P. Nezis, and H. Stenmark. 2014. Association of CHMP4B and autophagy with micronuclei: implications for cataract formation. *BioMed Res. Int.* 2014:974393. https://doi.org/10.1155/2014/974393

Samwer, M., M.W.G. Schneider, R. Hoefler, P.S. Schmalhorst, J.G. Jude, J. Zuber, and D.W. Gerlich. 2017. DNA cross-bridging shapes a single nucleus from a set of mitotic chromosomes. *Cell.* 170:956–972.e23. https://doi.org/10.1016/j.cell.2017.07.038

Santos, R.A., A.C. Teixeira, M.B. Mayorano, H.H.A. Carrara, J.M. Andrade, and C.S. Takahashi. 2010. Basal levels of DNA damage detected by micronuclei and comet assays in untreated breast cancer patients and healthy women. *Clin. Exp. Med.* 10:87–92. https://doi.org/10.1007/s10238-009-0079-4

Sanyal, S., and K.S. Krishnan. 2012. Genetic modifiers of comatose mutations in Drosophila: insights into neuronal NSF (N-ethylmaleimide-sensitive fusion factor) functions. *J. Neurogenet.* 26:348–359. https://doi.org/10.3109/01677063.2012.697500

Schindelin, J., I. Arganda-Carreras, E. Frise, V. Kaynig, M. Longair, T. Pietzsch, S. Preibisch, C. Rueden, S. Saalfeld, B. Schmid, et al. 2012. Fiji: an open-source platform for biological-image analysis. *Nat. Methods.* 9:676–682. https://doi.org/10.1038/nmeth.2019

Schooley, A., B. Vollmer, and W. Antonin. 2012. Building a nuclear envelope at the end of mitosis: coordinating membrane reorganization, nuclear pore complex assembly, and chromatin de-condensation. *Chromosoma.* 121:539–554. https://doi.org/10.1007/s00412-012-0388-3

Shumaker, D.K., K.K. Lee, Y.C. Tanhehco, R. Craigie, and K.L. Wilson. 2001. LAP2 binds to BAF.DNA complexes: requirement for the LEM domain and modulation by variable regions. *EMBO J.* 20:1754–1764. https://doi.org/10.1093/emboj/20.7.1754

Stephens, P.J., C.D. Greenman, B. Fu, F. Yang, G.R. Bignell, L.J. Mudie, E.D. Pleasance, K.W. Lau, D. Beare, L.A. Stebbings, et al. 2011. Massive genomic rearrangement acquired in a single catastrophic event during cancer development. *Cell.* 144:27–40. https://doi.org/10.1016/j.cell.2010.11.055

Stewénius, Y., L. Gorunova, T. Jonson, N. Larsson, M. Höglund, N. Mandahl, F. Mertens, F. Mitelman, and D. Gisselsson. 2005. Structural and numerical chromosome changes in colon cancer develop through telomere-mediated anaphase bridges, not through mitotic multipolarity. *Proc. Natl. Acad. Sci. USA.* 102:5541–5546. https://doi.org/10.1073/pnas.0408454102

Sullivan, W., A. Ashburner, and R.S. Hawley. 2000. Drosophila Protocols. Cold Spring Harbor Laboratory Press, Cold Spring Harbor, NY.

Sweeney, N.T., J.E. Brenman, Y.N. Jan, and F.B. Gao. 2006. The coiled-coil protein shrub controls neuronal morphogenesis in Drosophila. *Curr. Biol.* 16:1006–1011. https://doi.org/10.1016/j.cub.2006.03.067

Terradas, M., M. Martín, L. Hernández, L. Tusell, and A. Genescà. 2012. Nuclear envelope defects impede a proper response to micronuclear DNA lesions. *Mutat. Res.* 729:35–40. https://doi.org/10.1016/j.mrfmmm.2011.09.003

Terradas, M., M. Martín, L. Tusell, and A. Genescà. 2009. DNA lesions sequestered in micronuclei induce a local defective-damage response. *DNA Repair (Amst.).* 8:1225–1234. https://doi.org/10.1016/j.dnarep.2009.07.004

Thompson, S.L., and D.A. Compton. 2008. Examining the link between chromosomal instability and aneuploidy in human cells. *J. Cell Biol.* 180:665–672. https://doi.org/10.1083/jcb.200712029

Thurmond, J., J.L. Goodman, V.B. Strelets, H. Attrill, L.S. Gramates, S.J. Marygold, B.B. Matthews, G. Millburn, G. Antonazzo, V. Trovisco, et al. FlyBase Consortium. 2019. FlyBase 2.0: the next generation. *Nucleic Acids Res.* 47(D1):D759–D765. https://doi.org/10.1093/nar/gky1003

Vietri, M., K.O. Schink, C. Campsteijn, C.S. Wegner, S.W. Schultz, L. Christ, S.B. Thoresen, A. Brech, C. Raiborg, and H. Stenmark. 2015. Spastin and ESCRT-III coordinate mitotic spindle disassembly and nuclear envelope sealing. *Nature.* 522:231–235. https://doi.org/10.1038/nature14408

Voeltz, G.K., W.A. Prinz, Y. Shibata, J.M. Rist, and T.A. Rapoport. 2006. A class of membrane proteins shaping the tubular endoplasmic reticulum. *Cell.* 124:573–586. https://doi.org/10.1016/j.cell.2005.11.047

Walther, T.C., A. Alves, H. Pickersgill, I. Loïodice, M. Hetzer, V. Galy, B.B. Hülsmann, T. Köcher, M. Wilm, T. Allen, et al. 2003. The conserved Nup107-160 complex is critical for nuclear pore complex assembly. *Cell.* 113:195–206. https://doi.org/10.1016/S0092-8674(03)00235-6

Wang, L.Y., and H.J. Kung. 2012. Male germ cell-associated kinase is overexpressed in prostate cancer cells and causes mitotic defects via deregulation of APC/CCDH1. *Oncogene.* 31:2907–2918. https://doi.org/10.1038/onc.2011.464

Warecki, B., and W. Sullivan. 2018. Micronuclei Formation Is Prevented by Aurora B-Mediated Exclusion of HP1a from Late-Segregating Chromatin in Drosophila. *Genetics.* 210:171–187. https://doi.org/10.1534/genetics.118.301031

Webster, B.M., D.J. Thaller, J. Jäger, S.E. Ochmann, S. Borah, and C.P. Lusk. 2016. Chm7 and Heh1 collaborate to link nuclear pore complex quality control with nuclear envelope sealing. *EMBO J.* 35:2447–2467. https://doi.org/10.15252/embj.201694574

Wickham, H. 2016. ggplot2: Elegant Graphics for Data Analysis. Springer-Verlag, New York.

Willan, J., A.J. Cleasby, N. Flores-Rodriguez, F. Stefani, C. Rinaldo, A. Pisciottani, E. Grant, P. Woodman, H.E. Bryant, and B. Ciani. 2019. ESCRT-III is necessary for the integrity of the nuclear envelope in micronuclei but is aberrant at ruptured micronuclear envelopes generating damage. *Oncogenesis.* 8:29. https://doi.org/10.1038/s41389-019-0136-0

Yao, C., C. Wang, Y. Li, M. Zavortink, V. Archambault, J. Girton, K.M. Johansen, and J. Johansen. 2018. Evidence for a role of spindle matrix formation in cell cycle progression by antibody perturbation. *PLoS One.* 13:e0208022. https://doi.org/10.1371/journal.pone.0208022

Zhang, C.Z., A. Spektor, H. Cornils, J.M. Francis, E.K. Jackson, S. Liu, M. Meyerson, and D. Pellman. 2015. Chromothripsis from DNA damage in micronuclei. *Nature.* 522:179–184. https://doi.org/10.1038/nature14493

Zink, D., A.H. Fisher, and J.A. Nickerson. 2004. Nuclear structure in cancer cells. *Nat. Rev. Cancer.* 4:677–687. https://doi.org/10.1038/nrc1430
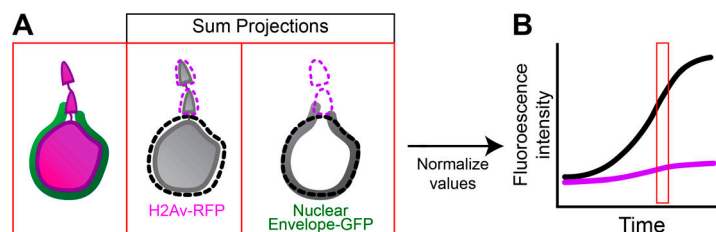
Supplemental material

Figure S1. **Schematic of fluorescence intensity quantification. (A)** Diagram illustrating where fluorescence intensity quantifications were measured. A region of interest was drawn around the nucleus (dashed black line) and each acentric (dashed purple lines). The fluorescence intensity of the nuclear envelope marker was then measured. Values were normalized (see Materials and methods). **(B)** Theoretical graph depicting the normalized fluorescence intensity on nuclei (black line) and acentrics (purple line) over time. The red box represents the hypothetical values measured from A. See also Figs. 3 and 4.
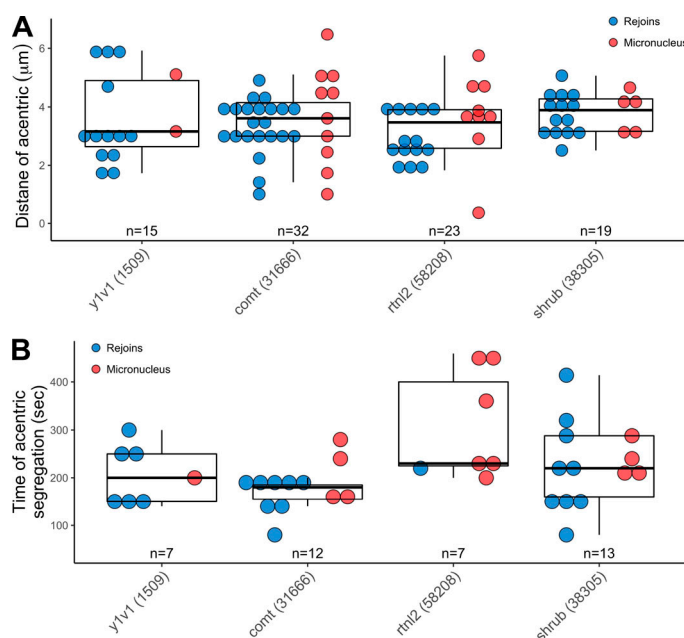

Figure S2. **Micronuclei formation is not correlated to changes in distance of acentrics from nuclei or time of acentric segregation. (A and B)** Comparison of the distances of acentrics from daughter nuclei (A; control, $n = 15$; Comt RNAi, $n = 32$; Rtnl2 RNAi, $n = 23$; Shrub RNAi, $n = 19$) and the times between anaphase onset and acentric segregation (B; control, $n = 7$; Comt RNAi, $n = 12$; Rtnl2, $n = 7$; Shrub RNAi, $n = 13$). Each dot represents one acentric. Blue dots represent acentrics that rejoin daughter nuclei. Red dots represent acentrics that form micronuclei. For each condition, there is no strong correlation between acentrics that form micronuclei and how far acentrics are from main nuclei at the time of acentric segregation. For each condition, there is no strong correlation between acentrics that form micronuclei and how long after anaphase acentrics began to segregate. Boxes represent interquartile ranges and lines represent medians of the measured data. There were no statistically significant differences between either the distance of acentrics from nuclei (Comt RNAi, $P = 0.9$; Rtnl2 RNAi, $P = 0.7$; Shrub RNAi, $P = 0.3$; two-sided Mann–Whitney–Wilcoxon tests) or the time of acentric segregation (Comt RNAi, $P = 0.3$; Rtnl2 RNAi, $P = 0.07$; Shrub RNAi, $P = 0.6$; independent two-sided t tests) between control and RNAi depleted neuroblasts. See also Fig. 5.
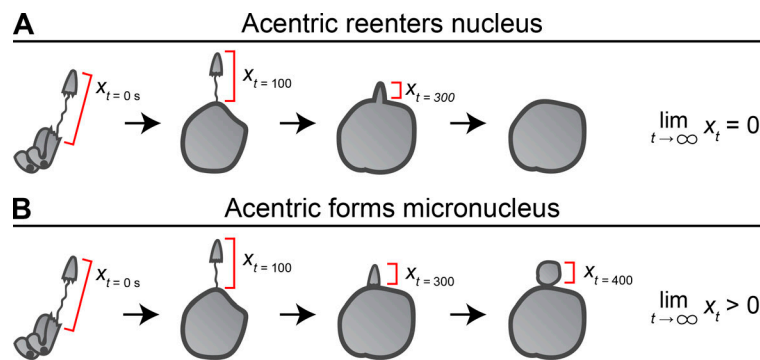
Figure S3. **Schematic detailing the measured distance between acentrics and daughter nuclei as acentrics segregate toward nuclei. (A)** Diagram illustrating that acentrics rejoining daughter nuclei will have a decreasing distance between the tail of the acentric and the closest point on the daughter nucleus. As time progresses, and the acentric completely reenters the daughter nucleus, the distance between the tail of the acentric and the daughter nucleus will approach 0. **(B)** Diagram illustrating that acentrics forming micronuclei will have a decreasing distance between the tail of the acentric and the closest point on the daughter nucleus until the acentric reaches the location where it is incapable of entering the daughter nucleus. As time progresses, the acentric will remain distinct from the main nucleus, and the distance between the tail of the acentric and the daughter nucleus will be measured as >0. See also Fig. 5.
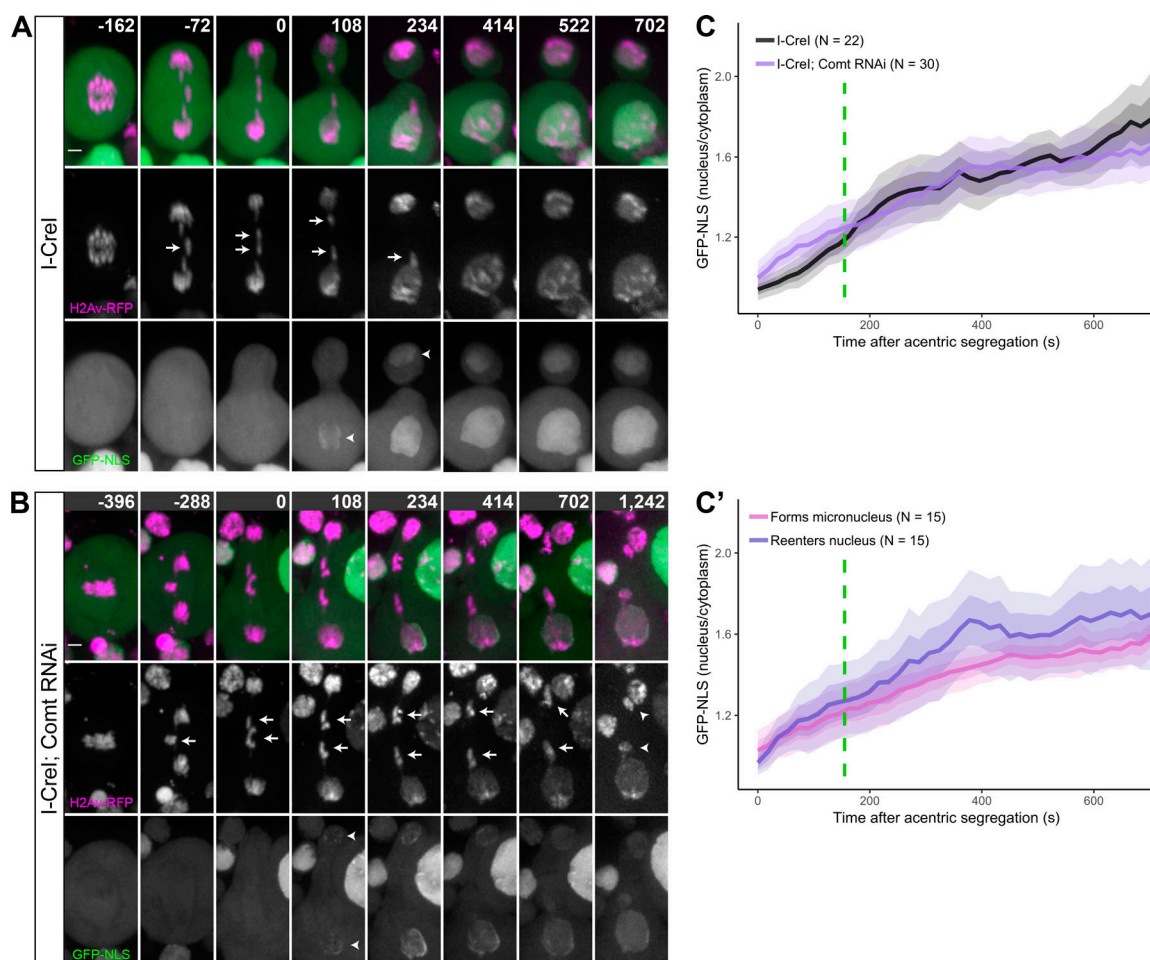
Figure S4. **Comt depletion results in acentric failure to enter nuclei and nuclear envelope reassembly defects. (A and B)** Stills from time-lapse videos of mitotic neuroblasts expressing H2Av-RFP (magenta), GFP-NLS (green), I-CreI with wild-type levels of Comt (A), or with RNAi-depleted levels of Comt (B). In control neuroblasts (A), acentrics (arrows) segregate poleward and enter daughter nuclei. Nuclei recruit GFP-NLS (arrowheads) while acentrics are still separate from nuclei. In Comt-depleted neuroblasts (B), acentrics segregate but fail to enter daughter nuclei, forming micronuclei (arrowheads). Nuclei recruit GFP-NLS while acentrics are still separate from nuclei, although GFP-NLS signal is not as strong or evenly distributed as it is in nuclei from control neuroblasts. Time is written in seconds after initial acentric poleward movement. Scale bars are 2 μm. **(C)** GFP-NLS intensity on daughter nuclei from control neuroblasts (black line; $n = 22$) and neuroblasts expressing RNAi against Comt (purple line; $n = 30$). Lines represent averages. Dark-shaded regions represent ± the standard error. Light-shaded regions represent ± twice the standard error. Dashed lines indicate time of nuclear envelope reassembly initiation. On average, nuclear envelope reassembly initiated at a comparable rate in control neuroblasts and neuroblasts with Comt RNAi. However, GFP-NLS intensity plateaued on nuclei from Comt-depleted divisions compared with control divisions, resulting in overall less signal intensity. Dashed green line represents average time that acentrics began to enter channels (155 s). **(C')** GFP-NLS intensity on neuroblasts expressing RNAi against Comt where acentrics reentered daughter nuclei (blue line; $n = 15$) or where acentrics formed micronuclei (pink line; $n = 15$). GFP-NLS signal intensity was lower on daughter nuclei from Comt-depleted neuroblasts when acentrics formed micronuclei than from Comt-depleted neuroblasts when acentrics reentered nuclei. Dashed green line represents average time that acentrics began to enter channels (155 s). Difference was determined to not be statistically significant ($P = 0.17$) by a Scheirer–Ray–Hare test. See also Fig. 5.

Video 1. **Acentric velocity decreases as acentrics pass through nuclear envelope channels.** Maximum projection of a spinning-disk confocal video of a mitotic neuroblast expressing I-CreI, H2Av-RFP (magenta), and Lamin-GFP (green). Scale bar is 2 μm. Time is written as seconds after initial acentric segregation. Frames were collected every 18 s. Frame rate is 15 frames/s. Video corresponds to Fig. 1 F.

Video 2. **Lamin extends from nuclear envelope channels and retracts as acentrics enter daughter nuclei.** Maximum projection of a spinning-disk confocal video of a mitotic neuroblast expressing I-CreI, H2Av-RFP (magenta), and Lamin-GFP (green). Scale bar is 2 μm. Time is written as seconds after initial acentric segregation. Frames were collected every 18 s. Frame rate is 15 frames/s. Video corresponds to Fig. 2 A.

Video 3.   Late-segregating acentrics are largely free of lamin. Maximum projection of a spinning-disk confocal video of a mitotic neuroblast expressing I-CreI, H2Av-RFP (magenta), and Lamin-GFP (green). Scale bar is 2 μm. Time is written as seconds after initial acentric segregation. Frames were collected every 18 s. Frame rate is 15 frames/s. Video corresponds to Fig. 3 A.

Video 4.   Late-segregating acentrics are largely free of nuclear pore complexes. Maximum projection of a spinning-disk confocal video of a mitotic neuroblast expressing I-CreI, H2Av-RFP (magenta), and GFP-Nup107 (blue). Scale bar is 2 μm. Time is written as seconds after initial acentric segregation. Frames were collected every 18 s. Frame rate is 15 frames/s. Video corresponds to Fig. 3 B.

Video 5.   Late-segregating acentrics are encompassed by nuclear membrane. Maximum projection of a spinning-disk confocal video of a mitotic neuroblast expressing I-CreI, H2Av-RFP (magenta), and PDI-GFP (yellow). Scale bar is 2 μm. Time is written as seconds after initial acentric segregation. Frames were collected every 18 s. Frame rate is 15 frames/s. Video corresponds to Fig. 4 A.

Video 6.   Late-segregating acentrics enter daughter nuclei in control neuroblast divisions. Maximum projection of a spinning-disk confocal video of a mitotic neuroblast expressing I-CreI and H2Av-RFP. Scale bar is 2 μm. Time is written as seconds after initial acentric segregation. Frames were collected every 10 s. Frame rate is 15 frames/s. Video corresponds to Fig. 5 A.

Video 7.   Late-segregating acentrics fail to enter nuclei in Comt-depleted neuroblasts. Maximum projection of a spinning-disk confocal video of a mitotic neuroblast expressing I-CreI, H2Av-RFP, and RNAi against Comt. Scale bar is 2 μm. Time is written as seconds after initial acentric segregation. Frames were collected every 10 s. Frame rate is 15 frames/s. Video corresponds to Fig. 5 B.

Video 8.   Late-segregating acentrics fail to enter nuclei in Rtnl2-depleted neuroblasts. Maximum projection of a spinning-disk confocal video of a mitotic neuroblast expressing I-CreI, H2Av-RFP, and RNAi against Rtnl2. Scale bar is 2 μm. Time is written as seconds after initial acentric segregation. Frames were collected every 10 s. Frame rate is 15 frames/s. Video corresponds to Fig. 5 C.

Video 9.   Late-segregating acentrics fail to enter nuclei in Shrub-depleted neuroblasts. Maximum projection of a spinning-disk confocal video of a mitotic neuroblast expressing I-CreI, H2Av-RFP, and RNAi against Shrub. Scale bar is 2 μm. Time is written as seconds after initial acentric segregation. Frames were collected every 10 s. Frame rate is 15 frames/s. Video corresponds to Fig. 5 D.

Video 10.   Shrub localizes to late-segregating acentrics as they reintegrate into daughter nuclei. Maximum projection of a spinning-disk confocal video of a mitotic neuroblast expressing I-CreI, H2Av-RFP (magenta), and Shrub-GFP (green). Scale bar is 2 μm. Time is written as seconds after initial acentric segregation. Frames were collected every 18 s. Frame rate is 15 frames/s. Video corresponds to Fig. 6 A.